



JGR Oceans

RESEARCH ARTICLE

10.1029/2022JC019065

Special Section:

Community Earth System Model High-Resolution (CESM-HR) Special Collection

Key Points:

- Sea surface temperature (SST) biases are considerably reduced in high-resolution models compared to low-resolution models
- Nonlocal K-profile parameterization KPP mixing is an important factor in SST bias reduction
- Eddy vertical heat transport can modulate nonlocal KPP mixing in eddy-active regions

Supporting Information:

Supporting Information may be found in the online version of this article.

Correspondence to:

G. Xu, gaopxu@tamu.edu

Citation:

Xu, G., Chang, P., Ramachandran, S., Danabasoglu, G., Yeager, S., Small, J., et al. (2022). Impacts of model horizontal resolution on mean sea surface temperature biases in the Community Earth System Model. *Journal of Geophysical Research: Oceans*, 127, e2022JC019065. https://doi.org/10.1029/2022JC019065

Received 11 JUL 2022 Accepted 29 NOV 2022

Impacts of Model Horizontal Resolution on Mean Sea Surface Temperature Biases in the Community Earth System Model

Gaopeng Xu¹, Ping Chang^{1,2}, Sanjiv Ramachandran¹, Gokhan Danabasoglu³, Stephen Yeager³, Justin Small³, Qiuying Zhang¹, Zhao Jing^{4,5}, and Lixin Wu^{4,5}

¹Department of Oceanography, Texas A&M University, College Station, TX, USA, ²Department of Atmospheric Sciences, Texas A&M University, College Station, TX, USA, ³National Center for Atmospheric Research, Boulder, CO, USA, ⁴Laboratory for Ocean Dynamics and Climate, Qingdao Pilot National Laboratory for Marine Science and Technology, Qingdao, China, ⁵Key Laboratory of Physical Oceanography, Ministry of Education/Institute for Advanced Ocean Study/ Frontiers Science Center for Deep Ocean Multispheres and Earth System (DOMES)/College of Oceanic and Atmospheric Sciences, Ocean University of China, Qingdao, China

Abstract Impacts of model horizontal resolution on sea surface temperature (SST) biases are studied using high-resolution (HR) and low-resolution (LR) simulations with the Community Earth System Model (CESM) where the nominal resolutions are 0.1° for ocean and sea-ice and 0.25° for atmosphere and land in HR, and 1° for all component models in LR, respectively. Results show that, except within eastern boundary upwelling systems, SST is warmer in HR than LR. Globally averaged surface ocean heat budget analysis indicates that 1°C warmer global-mean SST in HR is mainly attributable to stronger nonlocal vertical mixing and shortwave heat flux, with the former prevailing over the latter in eddy-active regions. In the tropics, nonlocal vertical mixing is slightly more important than shortwave heat flux for the warmer SST in HR. Further analysis shows that the stronger nonlocal mixing in HR can be attributed to differences in both the surface heat flux and shape function strength used in the parameterization. In addition, the shape function shows a nonlinear relationship with surface heat flux in HR and LR, modulated by the eddy-induced vertical heat transport. The stronger shortwave heat flux in HR, on the other hand, is mainly caused by fewer clouds in the tropics. Finally, investigation of ocean advection reveals that the improved western boundary currents in HR also contribute to the reduction of SST biases in eddy-active regions.

Plain Language Summary Sea surface temperature (SST) is a key climate variable, through which the atmosphere and ocean are coupled. However, current generation climate models that have nominal horizontal resolutions of ∼1° generally produce colder-than-observation SST over much of the tropics and midlatitudes. Increasing model resolution to 0.25° or finer can help reduce this cold bias, but the underlying physics is not well understood. By analyzing high-resolution (HR) and low-resolution (LR) Community Earth System Model (CESM) simulations, we find that vertical turbulent processes, particularly the convective component, show dominant contributions to the improved SST bias in the tropics and midlatitudes. The difference in the convective flux between HR and LR CESM is partially attributable to the difference in the surface heat flux, and the other important contributing factor is the warmer subsurface temperature in HR CESM driven by the vertical eddy heat transport. Overall, this study highlights the importance of improving representation of ocean eddy and turbulent processes in climate models.

1. Introduction

Sea surface temperature (SST) is a critical field to get right in simulations of the climate system because it is the key variable linking changes in the ocean to the atmosphere. SST anomalies associated with the El Niño-Southern Oscillation (ENSO), the Pacific Decadal Variability (PDV) and the Atlantic Multidecadal Variability (AMV) are all capable of modulating extreme weather globally (Di Lorenzo & Mantua, 2016; McCabe et al., 2004; McPhaden et al., 2006). The mesoscale SST anomalies in the northwestern Pacific can also influence heavy rainfall in western North America (Liu et al., 2021). To date, SST is also among the best measured climate fields, with long-term, global coverage obtained by ships (Smith et al., 2019; Woodruff et al., 2005), mooring buoys (TAO/TRITON, PIRATA, RAMA), Argo floats (Roemmich et al., 2009), and satellites (Reynolds & Smith, 1994).

Despite the fact that SST data sets are extremely useful for understanding global climate, it is still challenging to decipher the physical processes that govern SST, such as the relative roles of ocean mixing and advection, which

© 2022. American Geophysical Union. All Rights Reserved.

XU ET AL. 1 of 25

21699991, 2022, 12, Downloaded from https://agpubds.onlinelibrary.wiley.com/doi/10.1029/2022JC019065, Wiley Online Library on [11/01/2025]. See the Terms and Conditions (https://onlinelibrary.wiley.com/terms-and-conditions) on Wiley Online Library for rules of use; OA articles are governed by the applicable Creative Commons Licessnand Conditions (https://onlinelibrary.wiley.com/terms-and-conditions) on Wiley Online Library for rules of use; OA articles are governed by the applicable Creative Commons Licessnand Conditions (https://onlinelibrary.wiley.com/terms-and-conditions) on Wiley Online Library for rules of use; OA articles are governed by the applicable Creative Commons Licessnand Conditions (https://onlinelibrary.wiley.com/terms-and-conditions) on Wiley Online Library for rules of use; OA articles are governed by the applicable Creative Commons Licessnand Conditions (https://onlinelibrary.wiley.com/terms-and-conditions) on Wiley Online Library for rules of use; OA articles are governed by the applicable Creative Commons Licessnand Conditions (https://onlinelibrary.wiley.com/terms-and-conditions) on Wiley Online Library for rules of use; OA articles are governed by the applicable Creative Commons Licessnand Conditions (https://onlinelibrary.wiley.com/terms-and-conditions) on Wiley Online Library for rules of use; OA articles are governed by the applicable Creative Commons Licessnand Conditions (https://onlinelibrary.wiley.com/terms-and-conditions) on Wiley Online Library for rules of use; OA articles are governed by the applicable Creative Commons Licessnand Conditions (https://onlinelibrary.wiley.com/terms-and-conditions) on Wiley Online Library for rules of use; OA articles are governed by the applicable Creative Commons Licessnand Conditions (https://onlinelibrary.wiley.com/terms-and-conditions) on Wiley Online Library for rules of use; OA articles are governed by the applicable Creative Commons Licessnand Conditions (https://onlinelibrary.wiley.com/terms-and-conditions) on Wiley Online Library for rule

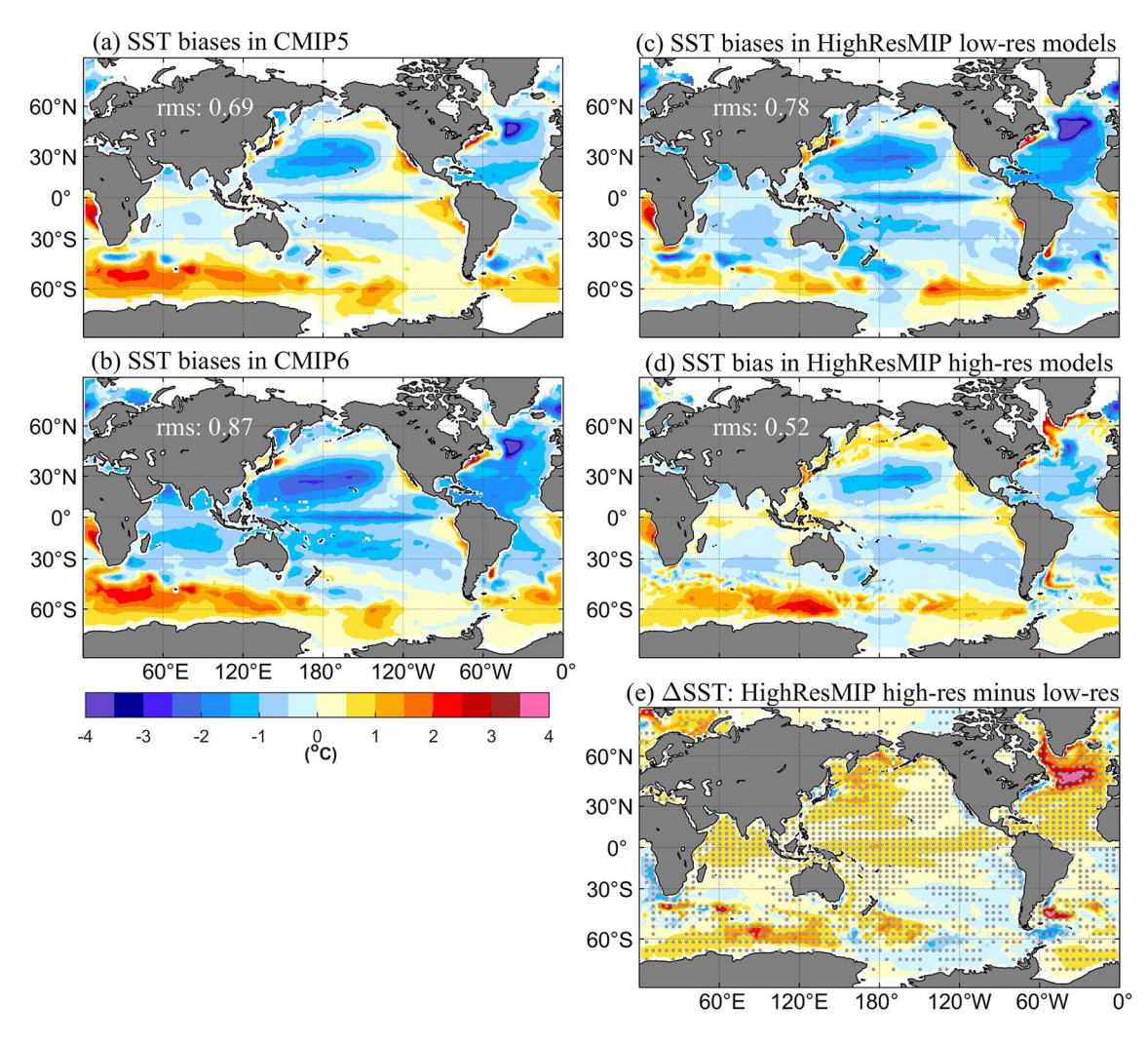


Figure 1. Sea surface temperature biases in (a) CMIP5 and (b) CMIP6, (c) HighResMIP low-resolution, and (d) high-resolution simulations. CMIP5 and CMIP6 biases are from the pre-industrial control simulations, usually 500 years long. For HighResMIP, 100-year-long 1950-control simulations are used. Climatological SST of HadISST1.0 (Rayner et al., 2003) for 1870–1900 and 1940–1970 is used in (a, b) and (c, d), respectively. (e) SST differences between HighResMIP high-resolution and low-resolution simulations (ΔSST). HadGEM3-GC3.1, ECMWF-IFS, CNRM-CM6-1, EC-Earth3P, CESM1.3, and AWI-CM1.1in HighResMIP are used. Stippling in (e) indicates that at least 4 out of 6 HighResMIP models agree on the sign of ΔSST. CMIP5 and CMIP6 models used here are listed in Tables S2 and S3 in Supporting Information S1.

are related to poorly observed details of ocean circulation and eddy formation. Numerical models have therefore become extremely important tools to study SST mechanisms. SST bias, defined as the departure of simulated long-term mean SST from observations, is an important metric to assess model performance. The Coupled Model Intercomparison Project (CMIP), which began in 1995, provides a platform to compare simulated climate across different models (https://www.wcrp-climate.org/wgcm-cmip). The climate models participating in CMIP Phase 5 (CMIP5), most of which have ocean and atmosphere horizontal resolutions of ~1°, show common biases in simulated climatological mean SST (Figure 1a). The biases can be divided into two groups: warm biases that primarily occur in the eastern boundary upwelling systems (EBUS), the Antarctic Circumpolar Current (ACC) region, and the east coasts of the U.S. and Japan; and cold biases that occur mainly in the Tropics (also known as the cold tongue bias) and midlatitudes.

The impacts of SST bias on the simulated climate system have been extensively studied in recent decades (Ashfaq et al., 2011; Camargo, 2013; Dutheil et al., 2020; He & Soden, 2016; Hsu et al., 2019; Garfinkel et al., 2020; Johnson et al., 2020; Large & Danabasoglu, 2006; Lee et al., 2018; McGregor et al., 2018). These studies show that climatological SST biases can strongly affect global precipitation distributions, as well as future projections of precipitation over ocean and land (Ashfaq et al., 2011; He & Soden, 2016; Johnson et al., 2020). In

XU ET AL. 2 of 25

addition, biases in tropical cyclone frequency, location, and intensity are strongly impacted by SST in the Tropics (Camargo, 2013; Dutheil et al., 2020; Hsu et al., 2019). Hsu et al. (2019) found that warm biases in the Pacific and cold biases in the Atlantic both can lead to overrepresentation of tropical cyclones in the Pacific. McGregor et al. (2018) also suggested that SST biases in the Atlantic basin can affect the wind and surface temperature in the Pacific via atmospheric teleconnections. Furthermore, the warm SST bias in the eastern tropical Pacific tends to cause a biased midlatitude stationary wave in the Southern Hemisphere through erroneous double Intertropical Convergence Zone (ITCZ) (Garfinkel et al., 2020). Lee et al. (2018) demonstrated that the SST bias in the Gulf Stream region can induce Rossby wave responses in the troposphere in the Northern Hemisphere. Moreover, Ying et al. (2019) showed that cold biases in the central equatorial Pacific can lead to La Niña-like warming patterns. Therefore, understanding the source of SST biases in models is vital for improving climate simulations and projections.

Gent et al. (2010) showed that warm biases in EBUS are significantly reduced after increasing the atmospheric resolution from 2° to 0.5° in the Community Climate System Model version 3.5 (CCSM3.5), pointing to the importance of atmospheric resolution in improving SST simulations in the upwelling regions. Xu et al. (2014) revealed that realistic coastal winds are important to reduce SST biases in the southeastern Atlantic. Based on three CCSM4 experiments with different atmospheric resolutions (0.5°, 1°, 2°), Small et al. (2015) showed that coastal wind stress curl is a dominant factor controlling SST biases via Sverdrup transport in EBUS, through its influence on poleward flow of warm tropical water. It was found that wind stress curl in 0.5° CCSM4 has a narrower coastal extent than in 1° and 2° CCSM4, leading to weaker poleward Sverdrup transport in 0.5° CCSM4 compared to 1° and 2° CCSM4 (Small et al., 2015). Kurian et al. (2021) demonstrated that improving the magnitude and spatial pattern of the Benguela coastal low-level jet plays a primary role in reducing SST biases in the Benguela upwelling region. In addition, coastal mountain topography, especially Andes, can also impact SST biases through low-level jet (Ma et al., 2019).

In contrast to the warm SST bias in EBUS, the source of cold SST biases in the tropics is still unclear. Song and Zhang (2009) found that SST biases are reduced after the convection schemes are modified in CCSM3, implying an important role for atmospheric convection processes. Li and Xie (2012) also argued that misrepresented cloud cover may be the main source of tropical SST biases in CMIP3 and CMIP5 models. Woelfle et al. (2018) presented evidence that the equatorial cold SST biases are directly generated by anomalous ocean advection driven by surface winds, which are sensitive to the underlying convection parameterization in the Community Earth System Model version 1 (CESM1). On the other hand, Moum et al. (2013) proposed that vertical ocean mixing can also modulate SST biases in the equatorial Pacific. Moreover, Vannière et al. (2014) argued that the tropical cold SST biases are advected into the tropics from extratropics. Burls et al. (2017) further showed that it is the subtropical cell that brings cold SST biases to the tropics.

Studies of cold biases in the midlatitudes, especially western boundary regions, are more recent and still remain sparse. Kirtman et al. (2012) illustrated that CCSM3.5 generates warmer SST in the western boundary current regions and Southern Ocean after increasing ocean resolution from 1° to 0.1° with the same atmosphere resolution of 0.5°. Small, Bacmeister, et al. (2014) performed high-resolution CESM simulations with atmosphere resolution of 0.25° and ocean resolution of 0.1° (hereafter HR), and found that SST biases in the western boundary currents are substantially reduced compared with low-resolution CESM with ocean and atmosphere resolution of 1° (hereafter LR). The reduced SST bias is mainly due to the finer ocean resolution (Small, pers. comm.). The ongoing High-Resolution Model intercomparison Project (HighResMIP, Haarsma et al., 2016) of CMIP6 is designed to further shed light on the impact of horizontal model resolution on climate simulations. Models participating in HighResMIP have ocean resolution finer than 0.25° and atmosphere resolution finer than 0.5°. Gutjahr et al. (2019) conducted a suite of experiments using the Max Planck Institute Earth System Model (MPI-ESM1.2) contribution to HighResMIP and showed that increasing atmosphere resolution tends to decrease SST almost globally while increasing ocean resolution tends to increase SST everywhere except in the upwelling regions. These results are consistent with previous studies using CCSM and CESM (Gent et al., 2010; Kirtman et al., 2012; Small, Bacmeister, et al., 2014; Small et al., 2015) as well as the Hadley Centre Global Environment Model 3—Global Coupled version 3.1 (HadGEM3-GC3.1; Roberts et al., 2019). However, the underlying mechanisms for midlatitude SST changes in HR models are still unclear, especially in eddy-active regions.

This study aims to investigate the impacts of model horizontal resolution on the representation of SST in the tropics and midlatitudes using a set of CESM simulations produced by the International Laboratory for High-resolution

XU ET AL. 3 of 25

Table 1
Models Participating in HighResMIP

Model	HadGEM3-GC3.1	ECMWF- IFS	CNRM-CM6-1	EC-Earth3P	CMCC- CM2-(V) HR4	MPI-ESM1.2	CESM1.3	AWI-CM1.1	
Resolution names	LL, HM, HH	LR, HR	LR, HR	LR, HR	HR4, VHR4	HR, XR	LR, HR	LR, HR	
Atmosphere model	MetUM-HadGEM3-GA7.1	IFS cy43r1	ARPEGE 6.3	IFS cy36r4	CAM4	ECHAM6.3	CAM5.2	ECHAM6.3.04p1	
Atmospheric horizontal resolution	2.5°, 0.5°, 0.5°	0.5°, 0.25°	2.5°, 1°	1°, 0.5°	1°, 0.25°	1°, 0.5°	1°, 0.25°	2.5°, 1°	
Atmosphere levels	85	91	91	91	26	95	30	47, 95	
Ocean model	NEMO-HadGEM3-GO6.0	NEMO3.4	NEMO3.6	NEMO3.6	NEMO3.6	MPIOM1.63	POP2	FESOM1.4	
Oceanic horizontal resolution	1°, 0.25°, 1/12°	1°, 0.25°	1°, 0.25°	1°, 0.25°	0.25°, 0.25°	0.5°, 0.5°	1°, 0.1°	0.5°, 0.25°	
Ocean levels	75	75	75	75	50	40	60, 62	46	
Note. Resolution names are defined independently across models.									

Earth System Prediction (iHESP), as well as seven other HighResMIP models. The CESM simulations follow the HighResMIP protocol (Haarsma et al., 2016) and represent CESM's contributions to HighResMIP. This manuscript is organized as follows. Models and methods are described in Section 2. SST biases in HR models are shown in Section 3. Section 4 presents a surface ocean heat budget analysis in HR and LR followed by an analysis of ocean mixing and advection in Section 5. Summary and discussion are given in Section 6.

2. Models and Methods

2.1. HighResMIP Simulations

In HighResMIP, ocean and sea-ice component models are all at least 0.25°, and atmosphere and land component models are almost all at least 0.5°. Among the eight participating models, there are six running at 0.25° in ocean and two running at 0.1° or finer (Table 1). Following the HighResMIP protocol, each of these models was used for two fully coupled simulations: (a) spinup-1950 (hereafter, SPIN)—a short (30–50 years) simulation starting from January ocean temperature and salinity (EN4.0; Good et al., 2013) averaged over the period of 1950–1954, (b) control-1950 (hereafter, CNTL)—a longer than 100-year continuation of SPIN with the same climate forcing corresponding to 1950 conditions (for details, refer to Figure 1 of Roberts et al., 2019). The following analysis will be mainly based on CNTL to investigate climatological SST biases.

HighResMIP models used in this study are: CMCC-CM2-(V)HR4 (Cherchi et al., 2019), ECMWF-IFS (Roberts et al., 2018), CNRM-CM6-1 (Voldoire et al., 2019), EC-Earth3P (Haarsma et al., 2020), HadGEM3-GC3.1 (Roberts et al., 2019), MPI-ESM1.2 (Gutjahr et al., 2019), CESM1.3 (Danabasoglu et al., 2012; Meehl et al., 2019; Small, Bacmeister, et al., 2014), and AWI-CM1.1 (Semmler et al., 2017). Resolutions of each model are shown in Table 1. Six of the eight HighResMIP models (HadGEM3-GC3.1, ECMWF-IFS, CNRM-CM6-1, EC-Earth3P, CESM1.3, and AWI-CM1.1) have configurations with different oceanic resolutions, which can be used to assess the role of ocean resolution in improving SST biases.

2.2. CESM

Given that we have access to full model output only from CESM but not from other models in HighResMIP, we will primarily analyze HR and LR CESM to address our scientific questions. In the following, we will particularly use HR and LR to refer to CESM simulations. CESM1.3 is an open source fully coupled climate model developed by the National Center for Atmospheric Research (NCAR). CESM1.3 is comprised of the Community Atmosphere Model version 5 (CAM5; Neale et al., 2010), the Parallel Ocean Program version 2 (POP2; Danabasoglu et al., 2012; Smith et al., 2010), the Community Land Model version 4 (CLM4; Lawrence et al., 2011) and the Community Ice Code version 4 (CICE4; Hunke & Lipscomb, 2008). As in Small, Bacmeister, et al. (2014), HR has a nominal resolution of 0.1° for POP2 and CICE4 and 0.25° for CAM5 and CLM4. In POP2, vertical mixing is represented by the K-Profile Parameterization (hereafter KPP; Large et al., 1994), which includes both local

XU ET AL. 4 of 25

21699291, 2022, 12, Downloaded from https

viley.com/doi/10.1029/2022JC019065, Wiley

and nonlocal mixing components. For more detailed descriptions of CESM1.3, we refer the reader to earlier studies (Chang et al., 2020; Danabasoglu et al., 2012; Meehl et al., 2019; Small, Bacmeister, et al., 2014).

LR is used for comparison with HR. LR has a nominal horizontal resolution of 1° for all component models, and the effects of mesoscale (10–100 km) and submesoscale (<10 km) eddies are included using the Gent and Mcwilliams (1990; hereafter GM90) and the Fox-Kemper et al. (2008; hereafter FK08) parameterizations in POP2. Both GM90 and FK08 are turned off in HR, however the same KPP vertical mixing is used in both HR and LR.

The 54-year HR SPIN simulation included an initial tuning phase of radiation imbalance at the top of atmosphere followed by several decades of integration, in accordance with the HighResMIP protocol. More information of model tuning process can be found in Chang et al. (2020). CNTL is a continuation of SPIN from year 55 to year 160 (hereafter CNTL-HR). For LR, only 30 years are used for SPIN, and CNTL is integrated from year 31 to year 181. To save on storage, only the first 20 years of SPIN output in HR (SPIN-HR) and LR (SPIN-LR) are saved. Since both SPIN-HR and SPIN-LR start from the same EN4.0 data set, comparing SPIN-HR and SPIN-LR allows us to examine the development of SST differences between HR and LR.

Because 20-year output of SPIN-HR and SPIN-LR is short to study the development of the SST biases, we performed a parallel 106-year LR integration to compare directly with CNTL-HR. This simulation was initialized by ocean temperature and salinity fields obtained from the first day of CNTL-HR, and thus is referred to as CNTL-LR-HRIC. Note that CNTL-HR and CNTL-LR-HRIC have the same initial condition for temperature and salinity. Therefore, we can examine the development of SST differences by comparing CNTL-HR and CNTL-LR-HRIC.

2.3. Methods

CESM employs a free surface configuration with a variable-thickness surface layer. As shown in the Chapter 5.2.1 of Smith et al. (2010), the temperature equation of the model surface layer is expressed as

$$\frac{\partial}{\partial t} \left(1 + \frac{\eta}{H} \right) T = -\frac{\partial u T}{\partial x} - \frac{\partial v T}{\partial y} + \frac{w T|_{-H}}{H} + \frac{Q_{\text{net}} - SW|_{-H}}{c_P \rho_0 H} + \kappa_H \left(\frac{\partial^2}{\partial x^2} + \frac{\partial^2}{\partial y^2} \right) T - \frac{\kappa_v}{H} \left(\frac{\partial T}{\partial z} - \gamma_x \right) |_{-H} + q_W T_W, \tag{1}$$

where η is sea surface height (SSH); T is potential temperature; u, v, and w are velocity along x, y, and z axes, respectively; H = 10 m; Q_{net} is the net surface heat flux including latent, sensible, longwave and shortwave heat flux at the surface, and the sign convention is that positive denotes heat flux into the ocean; $SW|_{-H}$ represents penetrative shortwave flux at z = -H; c_P is the ocean heat capacity taken as 3,996 J/kg/°C; ρ_0 is the density of sea water taken as 1,026 kg/m³; κ_H and κ_v are spatially varying horizontal and vertical diffusivity; and γ_x represents nonlocal turbulent heat transport in KPP. As eddies are not resolved in LR, total heat transport (uT, vT, wT) is taken as the sum of resolved transport and parameterized transport by GM90 and FK08.

To obtain Equation 1, the following approximations are employed: (a) the advective and diffusive horizontal fluxes between z=0 and $z=\eta$ are set to zero; (b) there is no advection of temperature across the surface with vertical velocity; (c) the freshwater flux is able to advect temperature across the surface $(q_W T_W)$. We have confirmed closure of Equation 1 budget, where the SSH term is much smaller than heat flux and mixing terms (see Figure S1 in Supporting Information S1). Therefore, it is reasonable to lump the SSH term together with mixing as the residual in the heat budget analyses if mixing is unavailable in the model output.

2.3.1. Spatial Surface Ocean Heat Budget

After integrating Equation 1 in time, the evolution of SST can be expressed as

$$T(t) - T(0) = \int_{0}^{t} \left(-\frac{\partial uT}{\partial x} - \frac{\partial vT}{\partial y} + \frac{wT|_{-H}}{H} \right) dt + \int_{0}^{t} \frac{Q_{\text{net}} - SW|_{-H}}{c_{P}\rho H} dt + \int_{0}^{t} \kappa_{H} \left(\frac{\partial^{2}}{\partial x^{2}} + \frac{\partial^{2}}{\partial y^{2}} \right) T dt - \int_{0}^{t} \frac{\kappa_{v}}{H} \left(\frac{\partial T}{\partial z} - \gamma_{x} \right) \Big|_{-H} dt - \left[\frac{\eta(t)}{H} T(t) - \frac{\eta(0)}{H} T(0) \right]. \tag{2}$$

XU ET AL. 5 of 25

21699291, 2022, 12, Downloaded from https://agupubs

Similar to Kurian et al. (2021), the equation of climatological mean SST can be obtained as

$$\frac{1}{t_0} \int_0^{t_0} T(t)dt - T(0) = \frac{1}{t_0} \int_0^{t_0} \int_0^t \left(-\frac{\partial uT}{\partial x} - \frac{\partial vT}{\partial y} + \frac{wT|_{-H}}{H} \right) + \kappa_H \left(\frac{\partial^2}{\partial x^2} + \frac{\partial^2}{\partial y^2} \right) T dt dt
+ \frac{1}{t_0} \int_0^{t_0} \int_0^t \frac{Q_{\text{net}} - SW|_{-H}}{c_P \rho H} dt dt + \frac{1}{t_0} \int_0^{t_0} \int_0^t \frac{\kappa_v}{H} \left(\frac{\partial T}{\partial z} - \gamma_x \right) \Big|_{-H} dt dt
- \frac{1}{t_0} \int_0^{t_0} \left[\frac{\eta(t)}{H} T(t) - \frac{\eta(0)}{H} T(0) \right] dt,$$
(3)

where t_0 is the length of the period of interest. Because the long-term mean of horizontal mixing is generally quite small compared with other near-surface terms, it will be lumped with the advection term together. The balance in Equation 3 will be referred to as the spatial surface ocean heat budget. The first two terms on the right-hand side comprise the ocean heat transport convergence (OHTC) followed by the atmospheric flux convergence (AFC) and ocean vertical mixing flux convergence (VMFC), as well as the SSH effect. VMFC is not available from CNTL-HR output, but it is available from SPIN-HR. Therefore, VMFC, along with the SSH term, will be calculated as the residual in CNTL-HR. To gain a complete understanding of ocean mixing in HR and LR, SPIN-HR and SPIN-LR will be used to discuss VMFC in detail.

2.3.2. Globally Averaged Surface Heat Budget

After taking a global average of Equation 2, the globally averaged SST can be expressed as

$$\langle T(t) \rangle - \langle T(0) \rangle = \int_{0}^{t} \frac{\langle wT|_{-H} \rangle}{H} dt + \int_{0}^{t} \frac{\langle Q_{\text{net}} \rangle - \langle SW|_{-H} \rangle}{c_{P}\rho H} dt - \int_{0}^{t} \left\langle \frac{\kappa_{v}}{H} \left(\frac{\partial T}{\partial z} - \gamma_{x} \right) \Big|_{-H} \right\rangle dt - \left[\left\langle \frac{\eta(t)}{H} T(t) \right\rangle - \left\langle \frac{\eta(0)}{H} T(0) \right\rangle \right], \tag{4}$$

where angle bracket < > represents a global average. The heat balance in Equation 4 is a function of time only because horizontal processes are eliminated by the global average. Globally averaged SST is controlled by the globally averaged: (a) vertical heat transport (VHTC), (b) AFC, (c) VMFC, and (d) SSH effect. Similar to the surface heat budget, the VMFC and SSH terms will be calculated as the residual due to their unavailability in CNTL-HR. Note that VMFC dominates the residual, which can be seen in the SPIN analyses in Section 4.

3. Mean SST in HighResMIP

Figures 1a and 1b show SST biases in CMIP5 and CMIP6 piControl simulations, where observed SST is taken from HadISST1.0 averaged over 1870–1900. This analysis includes 28 CMIP5 models and 34 CMIP6 models, whose information is shown in Tables S1 and S2 in Supporting Information S1, respectively. Most CMIP6 models have similar horizontal resolutions as their CMIP5 counterparts, around 1° in both atmosphere and ocean. It is evident that SST simulations show very little improvement from CMIP5 to CMIP6, and if anything a degradation, consistent with little change in model horizontal resolution.

Figure 1c shows the averaged SST biases from low-resolution versions of HadGEM3-GC3.1, ECMWF-IFS, CNRM-CM6-1, EC-Earth3P, CESM1.3 and AWI-CM1.1, where the first 100 years of CNTL are used. The observational benchmark used in Figure 1c is taken from HadISST1.0 averaged from 1940 to 1970, to match the 1950 forcing of the HighResMIP protocol. The results show similar bias patterns and magnitudes compared to the CMIP5 and CMIP6 piControl simulations, indicating that the climatological SST biases are not strongly sensitive to the choice of historical window.

Multi-model SST biases computed from 6 HighResMIP high-resolution simulations and the corresponding difference distributions between high-resolution and low-resolution simulations are shown in Figures 1d and 1e, respectively. It is evident that cold SST biases are reduced in most regions of the tropics and midlatitudes, but the bias turns from negative to positive in the high latitude North Pacific as well as near the equatorial Pacific and the equatorial Indian Ocean (Figure 1d), indicating overcorrections of SST biases in these regions. In addition, SST still shows warm biases in EBUS in high-resolution models (Figure 1d), even though the magnitude of the warm bias is significantly reduced in high-resolution models (Figure 1e), suggesting a positive impact of resolution increase on SST biases in all EBUS. As

XU ET AL. 6 of 25

discussed in Small et al. (2015) and Kurian et al. (2021), the bias improvements in EBUS mainly result from improved representation of the alongshore wind structures due to atmospheric resolution increase. Additionally, there is a noticeable improvement of SST biases in eddy-active regions, including the Kuroshio extension (KE), Gulf Stream extension (GSE), Agulhas current, and Brazil current regions (Figure 1e). Finally, the warm SST biases in the SubAntarctic region becomes worse in high-resolution models (Figures 1d and 1e), which may be related to net surface flux changes, especially cloud-related shortwave fluxes (Hyder et al., 2018). Overall, the RMS of SST has decreased from 0.78 in HighResMIP low-resolution simulations to 0.52 in the corresponding high-resolution simulations.

The magnitudes of cold bias in low-resolution simulations can be more than 4°C in the North Atlantic (Figures 1a–1c). As shown in Danabasoglu et al. (2010), SST in the North Atlantic is warmer in CCSM4 with Nordic Sea overflow parameterization than without overflow parameterization. Zhang et al. (2011) also pointed out that stronger Nordic Sea overflow can lead to warmer SST in the subpolar Atlantic, underscoring the importance of overflow representation for SST. Studies also showed positive correlation between SST bias in the North Atlantic and AMOC in CMIP5, implying smaller cold SST biases with stronger AMOC (Wang et al., 2014; Zhang & Zhao, 2015). Consistent with HighResMIP simulation, Marzocchi et al. (2015) also found better simulated SST in the North Atlantic in their 0.12° simulation than 0.25° and 1° simulations. The reduced cold SST bias in the North Atlantic could further reduce the deep ocean biases (Rackow et al., 2019). In addition, the warm SST biases off the east coasts of the U.S. and Japan, associated with incorrect paths of the Gulf Stream and Kuroshio currents, respectively, are largely improved in high-resolution models (Figures 1c and 1d).

As presented in Figure S2 in Supporting Information S1, HighResMIP models still show large variations in SST improvements with resolution. All show improvements of SST in EBUS after increasing the atmosphere horizontal resolution, especially MPI-ESM1-2 and CMCC-CM2. By contrast, only four of the six models with different oceanic resolution configurations (CESM1.3, HadGEM3-GC3.1, ECMWF-IFS, and AWI-CM1.1) have warmer SST in the Tropics and western boundary regions of midlatitudes. In addition, the magnitudes of SST difference between high-resolution and low-resolution simulations vary from model to model in the KE and GSE regions, ranging from about 0.5°C in ECMWF-IFS to 3°C in CESM1.3. CESM1.3 and AWI-CM1.1 share similar spatial pattern of SST differences between the high-resolution and low-resolution configurations, with large values in the Tropics and midlatitudes. In contrast, the largest impacts of horizontal model resolutions in HadGEM2-GC3.1 and ECMWF-IFS occur in the North Atlantic and the North Pacific. However, we can still see improvements of SST in the Tropics and midlatitudes in HadGEM2-GC3.1 and ECMWF-IFS. Given the consistency of impacts of horizonal resolutions on SST in the Tropics and midlatitudes across CESM1.3, HadGEM3-GC3.1, ECMWF-IFS, and AWI-CM1.1, it is appropriate to use CESM1.3 to study SST changes from LR to HR in the Tropics and midlatitudes.

Figure 2a shows SST difference between CNTL-HR and CNTL-LR-HRIC which is consistent with that shown in Figure S2 in Supporting Information S1. Globally averaged SST in CNTL-HR and CNTL-LR-HRIC are shown in Figure 2c. The global SST in CNTL-LR-HRIC (blue) is about 1°C cooler than CNTL-HR (red) after 30 years of integration. By the end of year 106, CNTL-LR-HRIC reaches a stable state with global-mean SST oscillating between 17.7 and 17.9°C, while CNTL-HR still shows a warming trend of \sim 0.2°C per century. As shown in Equations 2 and 4, SST is determined by $Q_{\rm net}$ and other oceanic processes. The $Q_{\rm net}$ difference between CNTL-HR and CNTL-LR-HRIC is shown in Figure 2b. Note that there is more heat loss from the ocean in CNTL-HR in the eddy-active regions. This strongly suggests that the warmer SST in CNTL-HR is mainly associated with oceanic processes instead of $Q_{\rm net}$ in eddy-active regions. But $Q_{\rm net}$ can be a candidate to explain the warmer SST in the Tropics. The 106-year mean of globally averaged $Q_{\rm net}$ is about 0.4 W/m² in CNTL-HR and 0.51 W/m² in CNTL-LR-HRIC (Figure 2d), indicating that the warmer globally averaged SST in CNTL-HR is due to oceanic processes.

SST and $Q_{\rm net}$ differences between SPIN-HR and SPIN-LR (Figure S3 in Supporting Information S1) are consistent with those between CNTL-HR and CNTL-LR-HRIC in the tropics and midlatitudes (Figures 2a and 2b), indicating robust SST bias is already generated within 20 years of integration. However, the negative SST differences are larger and broader in the 20-year SPIN experiments in the subpolar Pacific and SubAntarctic regions, suggesting that the system is still under adjustment.

Note that the temperature difference between CNTL-HR and CNTL-LR-HRIC is larger at 45 m than the surface (Figure S4 in Supporting Information S1). Therefore, it is better to take SST as the temperature at the first level of model instead of the average over the upper 50 m or so to study SST differences. To investigate the details of the physical processes controlling SST in the tropics and midlatitudes, heat budget analysis described in Section 2.3 will be applied to HR and LR in the next section.

XU ET AL. 7 of 25

21699291, 2022, 12, Downloaded from https://agupubs.onlinelibrary.wiley.com/doi/10.1029/2022JC019065, Wiley Online Library on [11/01/2025]. See the Terms and Conditions (https://onlinelibrary.wiley.com/doi/10.1029/2022JC019065, Wiley Online Library on [11/01/2025].

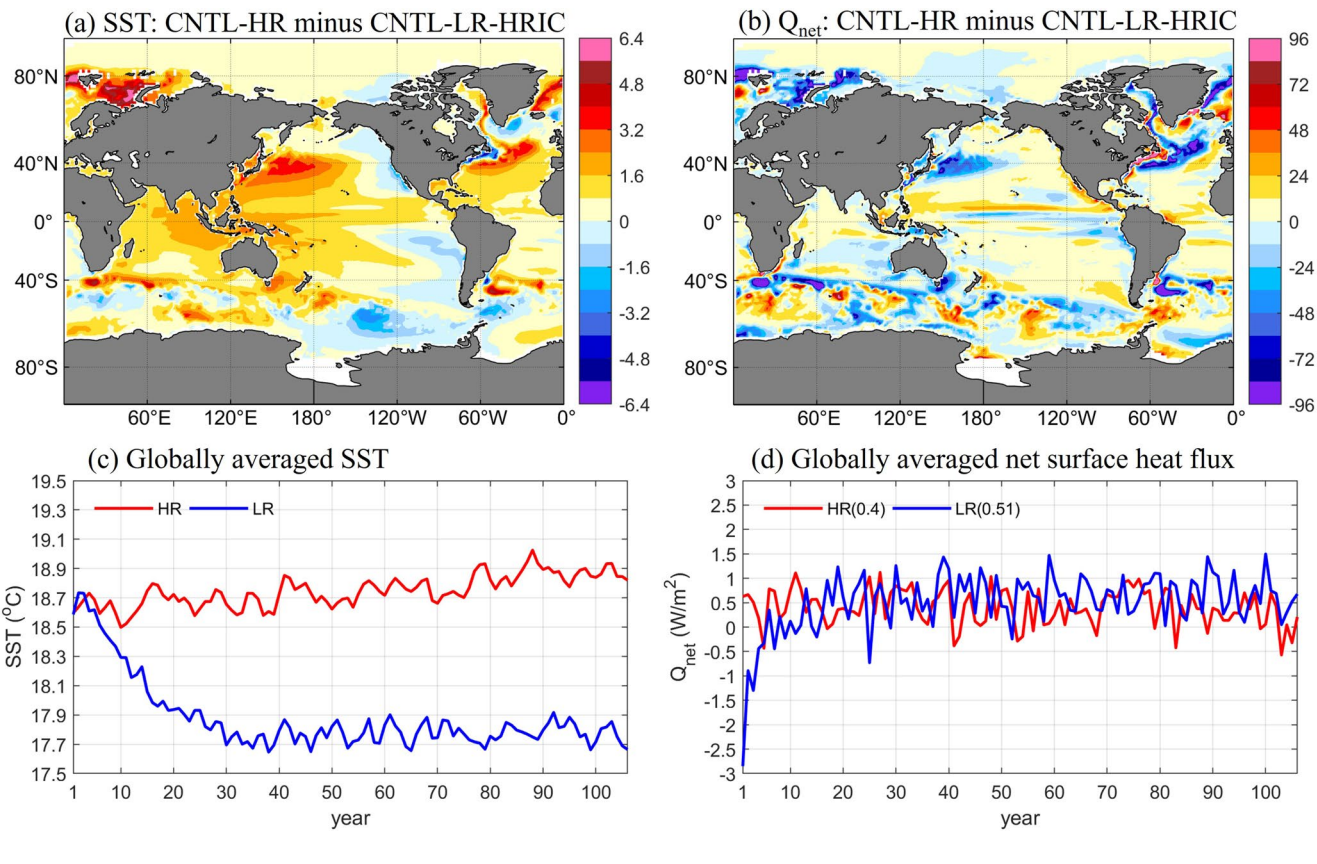


Figure 2. Differences of (a) sea surface temperature (SST) and (b) Q_{net} between CNTL-HR and CNTL-LR-HRIC (106 years mean); globally averaged (c) SST and (d) Q_{net} in CNTL-HR (red) and CNTL-LR-HRIC (blue). Numbers in brackets in (d) are the time mean of Q_{net} . Units: °C in (a) and W/m² in (b).

4. Heat Balance in CNTL-HR and CNTL-LR-HRIC

4.1. Globally Averaged Surface Heat Budget

To diagnose the causes of the 1°C warmer global-mean SST in CNTL-HR than in CNTL-LR-HRIC (Figure 2c), globally averaged surface ocean heat budget analysis (Equation 4) is conducted. As mentioned in Section 2, VMFC is calculated as the residual in CNTL-HR, as well as in CNTL-LR-HRIC for consistency. The residual should include both VMFC and SSH term, but be dominated by the former as discussed in Section 2.3. Therefore, the residual will be discussed as VMFC in the following. As shown in Figure 3a, the leading-order balance is between VMFC and AFC in CNTL-HR, with the latter broken down into non-shortwave heat flux AFC_tur (including sensible, latent, and longwave heat flux) and shortwave heat flux AFC_SW. Averaged over 106 years, AFC tends to cool down SST by 1916°C while VMFC and VHTC tend to warm up SST by 1,815 and 101°C, respectively (Figure 3a). The decomposition of AFC indicates that AFC_tur tends to cool down SST by 7,180°C, and this is partially compensated by AFC_SW with 5,264°C warming. Furthermore, the cooling induced by AFC_tur is mainly attributable to the heat release by evaporation (See Figure S5 in Supporting Information S1). Since the amplitude of SST change is much smaller than other terms, it is plotted in Figure 3 with a scaling factor of 10 to visually check its sign.

Figure 3b shows the difference of each term in the globally averaged heat balance (Equation 4) between CNTL-HR and CNTL-LR-HRIC. Averaged over the 106 years, global-mean SST in CNTL-HR is 0.86°C warmer than CNTL-LR-HRIC. It is also clear that the warming effects of VMFC and AFC_SW are stronger in CNTL-HR than CNTL-LR-HRIC, generating 104.58 and 148.31°C warmer SST in CNTL-HR, respectively. The differences in VMFC and AFC_SW account for 5.8% and 2.8% of the respective amplitude in CNTL-HR. In contrast, AFC_tur generates 237.36°C more cooling in CNTL-HR than CNTL-LR-HRIC, about 3.3% of cooling in CNTL-HR. The warming effect of VHTC is 14.68°C weaker in CNTL-HR than CNTL-LR-HRIC, showing a negative contribution to warmer global-mean SST in CNTL-HR. Therefore, vertical mixing is more important than other processes in generating warmer SST in CNTL-HR.

XU ET AL. 8 of 25

21699291, 2022, 12, Downloaded from https://agupubs.onlinelibrary.wiley.com/doi/10.1029/2022/C019065, Wiley Online Library on [11/01/2025]. See the Terms and Conditions (https://onlinelibrary.wiley.com/terms

and-conditions) on Wiley Online Library for rules of use; OA articles are governed by the applicable Creative Commons Licenso

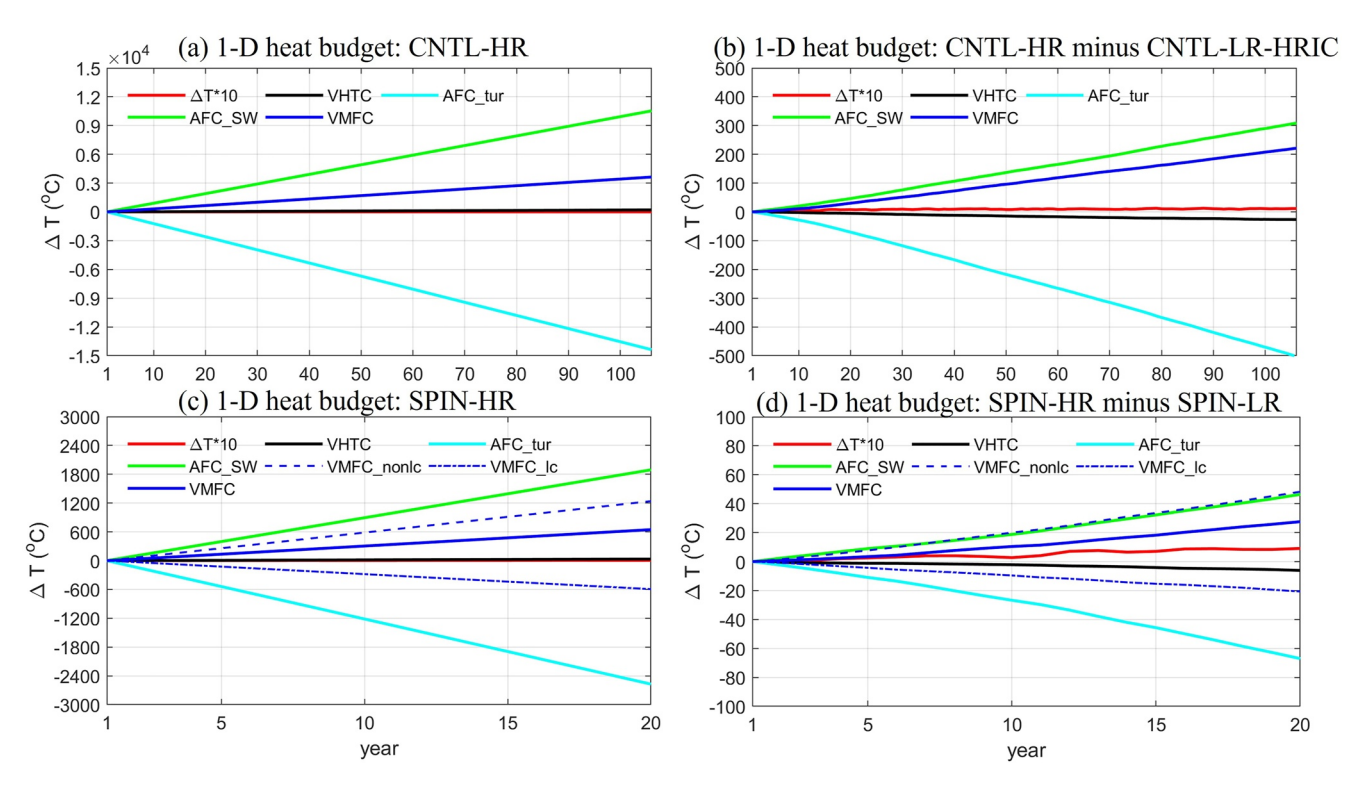


Figure 3. Heat budget of globally averaged sea surface temperature (SST) in (a) CNTL-HR, (b) CNTL-HR minus CNTL-LR-HRIC, (c) SPIN-HR, and (d) SPIN-HR minus SPIN-LR. Red for SST changes, black for VHTC, cyan for AFC_tur, green for AFC_SW, solid blue for VMFC, dashed blue for VMFC_nonlc, and dot-dashed blue for VMFC_lc. Units are °C. VMFC in (a, b) is obtained as the residual including SSH term, but not in (c, d). SSH term is absent in (c, d) because it is quite small. 1° C = 4.10×10^{6} J/m³, assuming a sea-water density of 1,026 kg/m³ and specific heat of 3,996 J/kg/°C over a 10 m upper ocean.

As shown in Large et al. (1994), vertical mixing parameterized by KPP includes local mixing (i.e., diffusive mixing, VMFC_lc) and nonlocal mixing (i.e., convective mixing, VMFC_nonlc). Diffusive mixing is proportional to the local vertical temperature gradient, while convective mixing is induced by convective instability within the boundary layer, which is nonzero only with unstable surface forcing. Therefore, the stronger warming induced by vertical mixing in HR is the net effect of the local and nonlocal mixing. To study the details of VMFC, the same globally averaged SST heat budget is also applied to the 20-year SPIN-HR and SPIN-LR (Figures 3c and 3d), in which the local and nonlocal KPP mixing terms were saved as model output. Solid lines in Figures 3c and 3d are exactly balanced and the two components of VMFC are represented by blue dashed lines. SPIN-HR and SPIN-LR essentially reproduce the results of CNTL-HR and CNTL-LR-HRIC, suggesting that we can use the shorter simulations from SPIN-HR and SPIN-LR to further decompose vertical mixing into local and nonlocal components and investigate the detailed processes contributing to the SST difference between HR and LR.

In SPIN-HR (Figure 3c), one can see that nonlocal vertical mixing (i.e., VMFC_nonlc) tends to warm up SST, but local vertical mixing (i.e., VMFC_lc) tends to cool down SST. Physically, VMFC_nonlc corresponds to convection when dense (cold) water is above lighter (warmer) water. Hence it tends to have a warming effect at the surface. VMFC_lc is primarily associated with diffusion of warm surface waters into the colder thermocline (hence a cooling effect). Compared with SPIN-LR, VMFC_nonlc and VMFC_lc are both stronger in SPIN-HR

Table 2Twenty-Year Average of Each Term in the Globally Averaged Heat Budget of SPIN-HR and SPIN-LR (Unit: °C)

			VN	ИFC			SSH
	ΔSST	VHTC	Local	Nonlocal	AFC_SW	AFC_tur	term
HR	0.32	17.31	-296.44	618.70	945.46	-1284.69	-0.02
LR	-0.18	20.05	-286.21	596.48	923.81	-1254.28	-0.03
HR-LR	0.50	-2.74	-10.23	22.22	21.65	-30.41	0.01

XU ET AL. 9 of 25

(Figure 3d). Table 2 shows the 20-year average of heat balance in SPIN-HR and SPIN-LR. SST in SPIN-HR is 0.5°C warmer than SPIN-LR, which is attributed to stronger VMFC_nonlc and AFC_SW. Contributions to the warmer SST from VMFC_nonlc and AFC_SW are 22.22 and 21.65°C, respectively, which account for 3.6% and 2.3% of the respective warming in SPIN-HR. Therefore, nonlocal vertical mixing is slightly more important than shortwave heat flux in generating warmer SST in HR simulations from a global average perspective. Further details of why nonlocal vertical mixing differs between HR and LR will be discussed in Section 5.

4.2. Spatial Surface Ocean Heat Budget

Looking at spatial distributions of surface ocean heat budget contributors is useful to examine how the balance among various terms governing SST differences between HR and LR varies across geographic locations. Similar to the globally averaged heat budget, there are three main factors contributing to the evolution of the SST heat budget (Equation 3): ocean advection (i.e., OHTC), atmosphere flux (i.e., AFC) and vertical mixing (i.e., VMFC). OHTC here includes both vertical and horizontal advection processes. Each term in Equation 3 (with t_0 as 106 years) in CNTL-HR and CNTL-LR-HRIC are shown in Figure 4, where VMFC is calculated as the residual with the small SSH term included.

As shown in Figure 4a, SST changes relative to the first year in CNTL-HR are small (less than 1°C) in 106 years. Consistent with the global-average heat budget (Figure 3a), the balance in spatial surface ocean heat budget is dominated by atmosphere forcing (Figure 4c) and vertical mixing (Figure 4d) over most of the global ocean. Ocean advection, OHTC, only shows large contributions in eddy-active regions (Figure 4b). Heat loss within the upper 10 m of the ocean occurs everywhere, except in the equatorial regions, EBUS, and some SubAntarctic regions (Figure 4c). The heat loss indicates that the net shortwave heat flux within the upper 10 m is less than the outgoing non-shortwave heat fluxes. Due to the large compensation among OHTC, AFC, and VMFC, the scale of SST change is much smaller than the other three, similar to the global-average heat budget.

The differences between CNTL-HR and CNTL-LR-HRIC are demonstrated in Figures 4e–4h. In much of the western and tropical basins, SST is warmer in CNTL-HR, especially in the eddy-active regions where the differences can reach 4°C (Figure 4e). The cooling induced by atmosphere flux is stronger in CNTL-HR in the eddy-active regions (Figure 4g), which is mainly contributed by the non-shortwave component AFC_tur (Figure 5b). On the other hand, shortwave heating (i.e., AFC_SW) is larger in CNTL-HR in the tropical and polar regions, but smaller in the EBUS and the Southern Ocean (Figure 5a), which is similar to the SST difference pattern in Figure 4e. The spatial correlation coefficient of SST difference (Figure 4e) and AFC_SW difference (Figure 5a) is 0.48, indicating that the shortwave heat flux and SST differences are closely related, but that other terms are involved. Like AFC_SW, ocean advection also shows stronger warming in CNTL-HR in eddy-active regions (Figure 4f). Vertical mixing differences (Figure 4h), which are the net effect of local and nonlocal components, show a nearly opposite pattern from atmosphere forcing (Figure 4g), with the pattern correlation coefficient of -0.9.

The relative importance of nonlocal versus local vertical mixing in the SST difference between HR and LR can be further investigated using direct model output from SPIN-HR and SPIN-LR. Figure S6 in Supporting Information S1 shows the results of a similar spatial surface ocean heat budget analysis using the 20-year simulations from SPIN-HR and SPIN-LR. Despite the shorter simulation length, the heat balance in SPIN-HR and SPIN-LR shows a very similar structure to that of CNTL-HR and CNTL-LR-HRIC. In both cases, ocean advection and vertical mixing are primarily responsible for the warmer SST in HR in eddy-active regions (Figure S6 in Supporting Information S1, Figure 4), and AFC_SW and VMFC for the warmer SST in tropical regions (Figure 5c). As in the globally averaged heat budget, the short SPIN simulations can offer insight into the spatial surface ocean heat budget differences seen in the CNTL simulations.

In SPIN-HR, local vertical mixing (i.e., VMFC_lc) tends to cool surface temperature except in high-latitude regions, and the strongest cooling occurs in equatorial regions (Figure 6a). In contrast, nonlocal vertical mixing (i.e., VMFC_nonlc) tends to warm up the surface layer, with large amplitudes in eddy-active regions (Figure 6b). An examination of the differences of these two terms between SPIN-HR and SPIN-LR shows that VMFC_nonlc is stronger in SPIN-HR in eddy-active and tropical regions, while the difference of VMFC_lc shows generally opposite sign to that of VMFC_nonlc (Figures 6c and 6d).

Figure 7a shows 20-year mean of area-averaged heat balance in four eddy-active regions shown by boxes in Figure 4f. Ocean advection (i.e., OHTC), nonlocal vertical mixing (i.e., VMFC_nonlc), and shortwave heating (i.e., AFC_SW) all work to warm the ocean surface in SPIN-HR (cyan) and SPIN-LR (blue), while local vertical mixing (i.e., VMFC_lc)

XU ET AL. 10 of 25

21699291, 2022, 12, Downloaded from https://agupubs.onlinelibrary.wiley.com/doi/10.1029/20221C019065, Wiley Online Library on [11/01/2023]. See the Terms and Conditions (https://onlinelibrary.wiley.com/terms-and-conditions) on Wiley Online Library for rules of use; OA articles are governed by the applicable Creative C

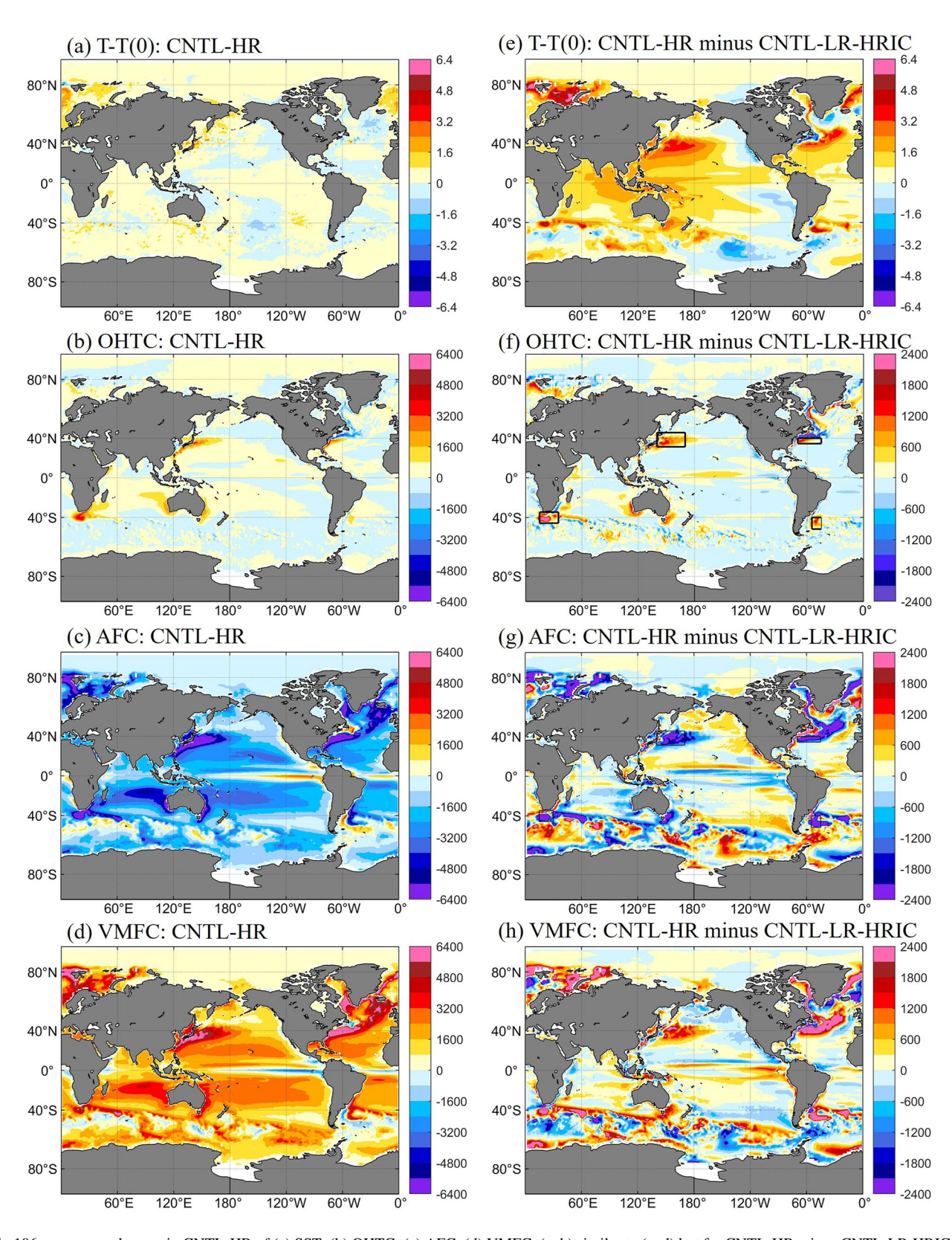


Figure 4. 106-year mean changes in CNTL-HR of (a) SST; (b) OHTC; (c) AFC; (d) VMFC. (e–h) similar to (a–d) but for CNTL-HR minus CNTL-LR-HRIC. Units are °C. The scale of (a) and (e) is smaller than other panels. Four boxes in (f) indicates eddy-active regions with large OHTC differences. $1^{\circ}C = 4.10 \times 10^{6} \text{ J/m}^{3}$, assuming a sea-water density of $1,026 \text{ kg/m}^{3}$ and specific heat of 3,996 J/kg/°C over a 10 m upper ocean.

XU ET AL. 11 of 25

21699291, 2022, 12, Downloaded from https://agupubs.onlinelibrary.wiley.com/doi/10.1029/2022IC019065, Wiley Online Library on [11/01/2025]. See the Terms and Conditions (https://onlinelibrary.wiley.com/doi/10.1029/2022IC019065, Wiley Online Library on [11/01/2025]. See the Terms and Conditions (https://onlinelibrary.wiley.com/doi/10.1029/2022IC019065, Wiley Online Library on [11/01/2025]. See the Terms and Conditions (https://onlinelibrary.wiley.com/doi/10.1029/2022IC019065, Wiley Online Library.on [11/01/2025]. See the Terms and Conditions (https://onlinelibrary.wiley.com/doi/10.1029/2022IC019065, Wiley Online Library.on [11/01/2025].

on Wiley Online Library for rules of use; OA articles are governed by the applicable Creative Commons Licens

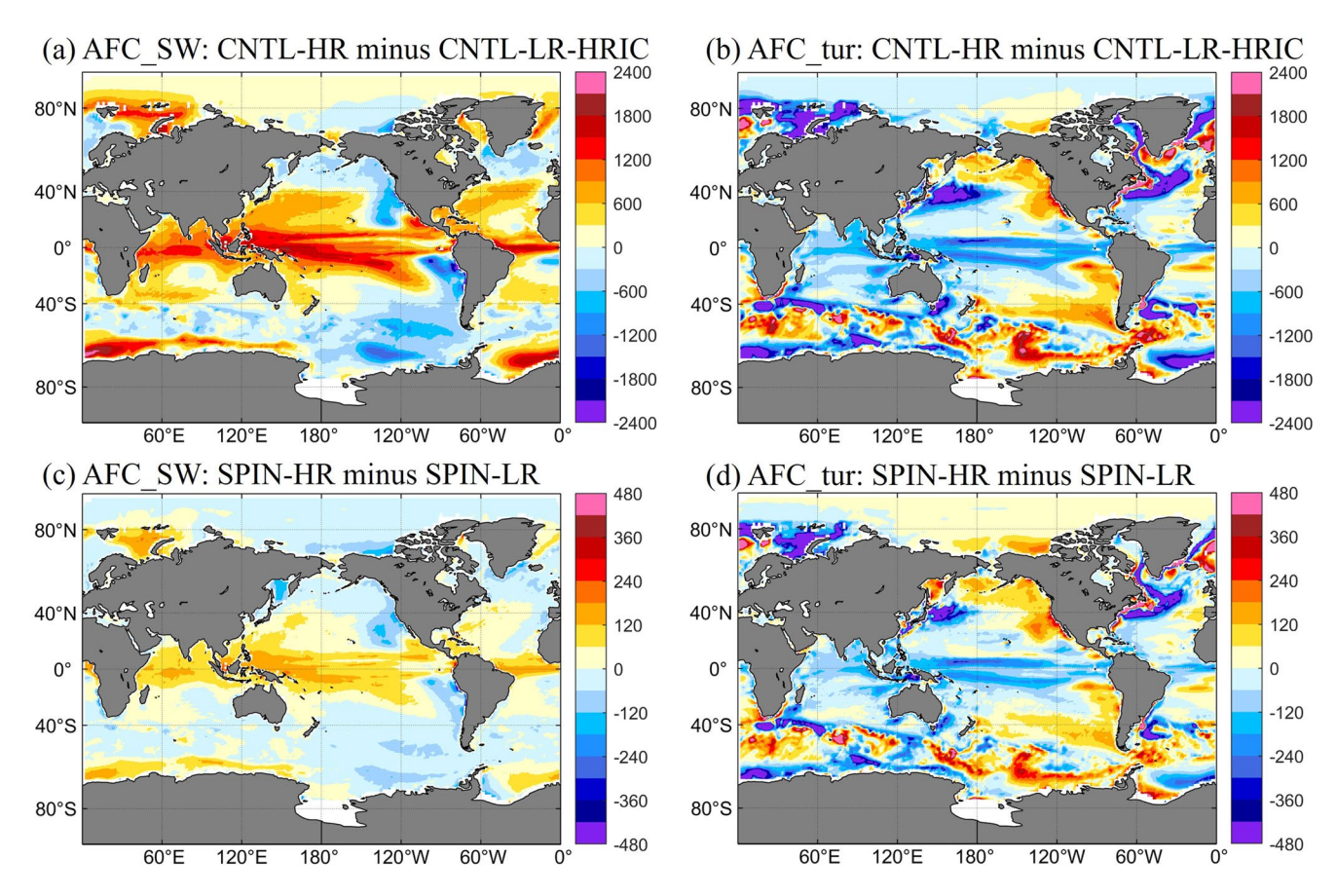


Figure 5. Difference of (a) AFC_SW and (b) AFC_tur between CNTL-HR and CNTL-LR-HRIC; (c) AFC_SW and (d) AFC_tur between SPIN-HR and SPIN-LR. Units: °C.

and non-shortwave heat flux (i.e., AFC_tur) work to cool it. SST is about 1.6°C warmer in SPIN-HR than SPIN-LR in these eddy-active regions (red in Figure 7a), which is considerably larger than the globally averaged difference of 0.5°C. The stronger non-shortwave heat flux in SPIN-HR tends to decrease SST, which is counterbalanced by the stronger nonlocal mixing, stronger ocean advection, stronger shortwave heating, and weaker local mixing. Again, SSH contributes to the SST difference much less than other processes. As a result, ocean advection and nonlocal vertical mixing are the two most dominant factors in generating warmer SST in eddy-active regions, while shortwave heating plays a secondary role. This result also holds in each eddy-active region as shown in Figure S7 in Supporting Information S1. Similar results from 106-year CNTL-HR and CNTL-LR-HRIC are shown in Figure S8a in Supporting Information S1, confirming that vertical mixing and advection are the most important for warmer SST in the eddy-active regions in HR. Zhu et al. (2020) found that SST in the North Pacific will get warmer after increasing the strength of convective mixing in the LR ocean-only Modular Ocean Model version 5 (MOM5), which supports the finding that convective mixing is important to reduce the cold SST biases.

In the tropics (30°S–30°N), ocean advection shows the smallest contribution to the heat budget in both SPIN-HR (cyan) and SPIN-LR (blue, Figure 7b). The SST in SPIN-HR is about 0.5°C warmer than SPIN-LR (red in Figure 7b), comparable to the global average of 0.5°C. Different from eddy-active regions, local vertical mixing is stronger in SPIN-HR than SPIN-LR in the tropics, generating cooler SST of 39.9°C, which is comparable with –53.4°C induced by stronger non-shortwave heat flux. In addition, nonlocal vertical mixing and shortwave heating are the only two processes contributing to warmer SST in SPIN-HR, producing 45.5 and 53.7°C warming, respectively. They account for 5.6% and 4.3% of the corresponding value in SPIN-HR. Therefore, nonlocal vertical mixing is relatively more important than shortwave heating for the warmer SST in the tropics in HR. On the other hand, because there is strong compensation between local vertical mixing (–39.9°C) and nonlocal vertical mixing (45.5°C), the net warming effect of vertical mixing is only 5.6°C, which is much smaller than shortwave heating. This is consistent with CNTL-HR and CNTL-LR-HRIC results shown in Figure S8b in Supporting Information S1.

XU ET AL. 12 of 25

21699291, 2022, 12, Downloaded from https://agupubs.onlinelibrary.wiley.com/doi/10.1029/2022JC019065, Wiley Online Library on [11/01/2025]. See the Terms and Conditions (https://online

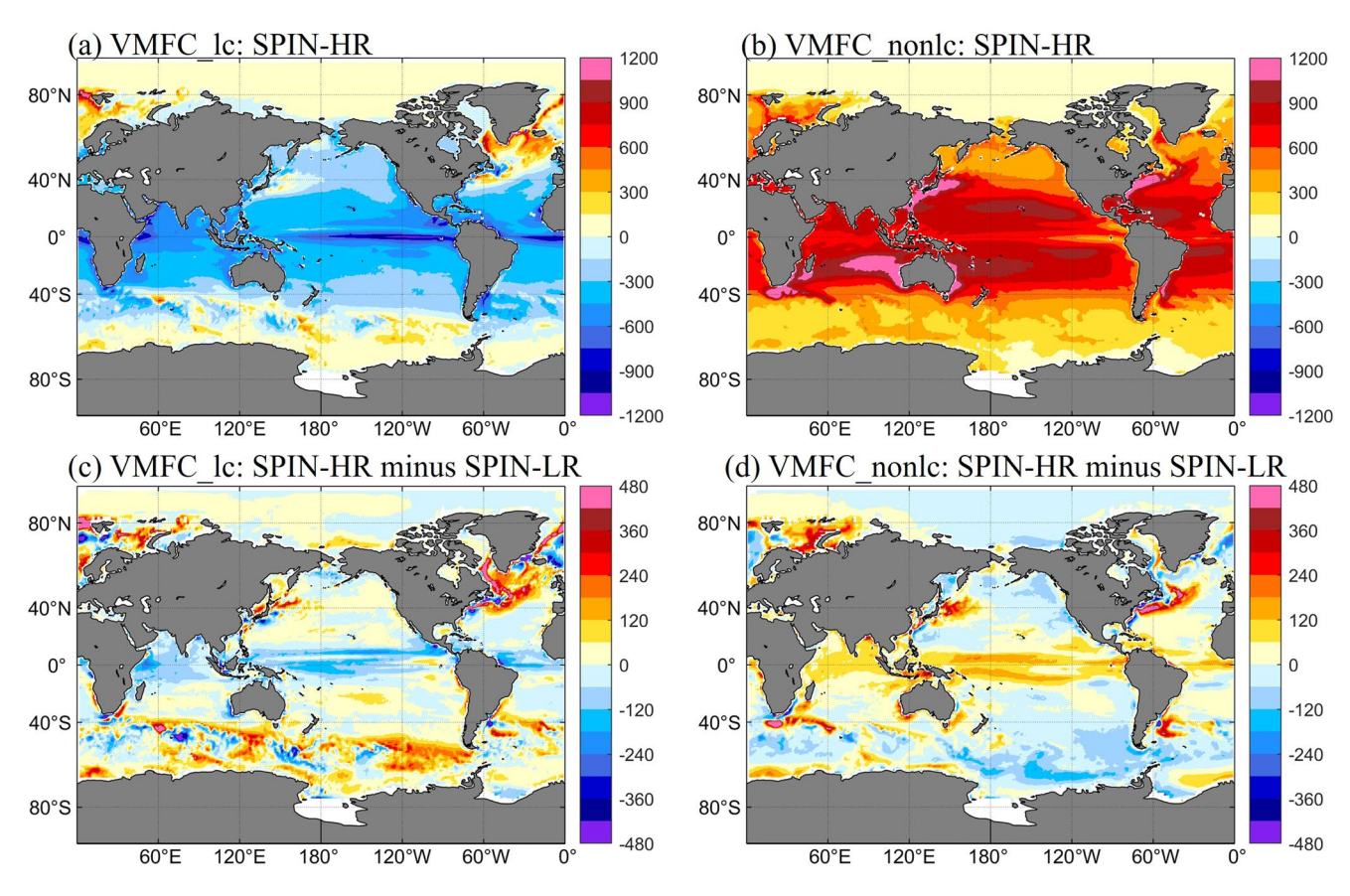


Figure 6. Breakdown of VMFC into (a) local and (b) nonlocal components in SPIN-HR. Difference of (c) VMFC_lc and (d) VMFC_nonlc between SPIN-HR and SPIN-LR. Units: °C.

As shown in Figure S9 in Supporting Information S1, there are less low cloud in regions where shortwave heat flux is larger in HR (Figures 5a and 5c), which may be related to impacts of model resolution on deep and shallow convection schemes in CAM5. We note that convection-related parameters in HR are kept the same as those in LR, which may be responsible for higher tropical precipitation in HR (Chang et al., 2020). Future exploration, which is beyond the scope of this work, is needed to investigate differences in parameterized clouds between HR and LR. In the next section, we will focus more on the causes of upper ocean vertical mixing and advection differences between SPIN-HR and SPIN-LR.

5. Vertical Mixing and Advection

5.1. Vertical Mixing

5.1.1. Importance of Shape Function

As shown in Large et al. (1994) and Van Roekel et al. (2018), nonlocal KPP flux is parameterized as $\kappa_z \gamma_x = C_* \kappa (c_s \kappa \varepsilon)^{1/3} G(\sigma) \overline{(wT)}_{\rm sfc}$, where C_*, κ, c_s , and ε are constants defined in Large et al. (1994). In the following discussion, $C_* \kappa (c_s \kappa \varepsilon)^{1/3}$ is expressed as C for convenience. The nonlocal KPP flux is non-zero only in regions of unstable stratification caused by surface buoyancy flux. Under the assumption that heat flux dominates surface buoyancy flux, unstable conditions in CESM occur when the net heat flux absorbed in the boundary layer is negative, indicating a net heat loss from the surface. $\overline{(wT)}_{\rm sfc}$ is the active surface kinematic fluxes, including the net longwave heat flux, sensible and latent heat flux (refer to Equation A2c in Large et al., 1994; hereafter, referred to as $Q_{\rm ns}$). In theory, shortwave radiation absorbed in the boundary layer (SWBL) can also contribute to the nonlocal KPP flux. Unfortunately, SWBL is not saved in SPIN-HR. However, Van Roekel et al. (2018) found

XU ET AL. 13 of 25

21699291, 2022, 12, Downloaded from https://agupubs.onlinelibrary.wiley.com/doi/10.1029/2022/C019065, Wiley Online Library on [11/01/2025]. See the Terms and Conditions (https://onlinelibrary.wiley.com/terms-

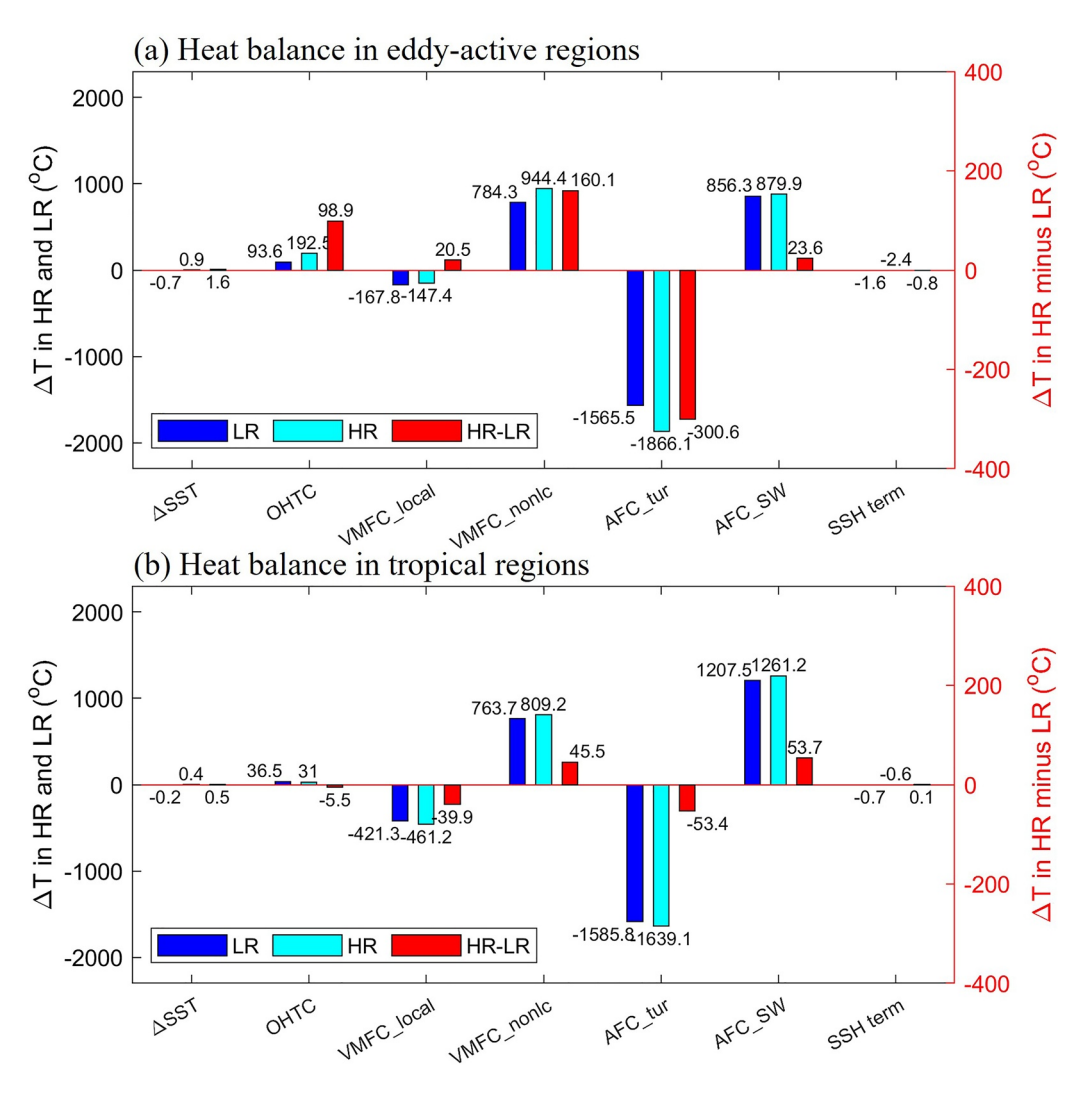


Figure 7. Twenty-year mean of heat balance (a) in 4 eddy-active regions labeled by black boxes in Figures 4f and (b) tropical regions (30°S–30°N). Blue for SPIN-LR, cyan for SPIN-HR and red for SPIN-HR minus SPIN-LR.

that nonlocal KPP flux is not sensitive to SWBL. Therefore, the nonlocal KPP flux will be discussed in terms of Q_{ns} in the following, and can be simply rewritten as

$$\kappa_z \gamma_x = CG(\sigma) Q_{\rm ns}. \tag{5}$$

 $G(\sigma)$ is the shape function expressed as a cubic polynomial

$$G(\sigma) = c_1 + c_2 \sigma + c_3 \sigma^2 + c_4 \sigma^3, \tag{6}$$

where $\sigma = -\frac{z}{h}$, $c_1 = 0$, $c_2 = 1$, $c_3 = -2 + 3G(1) - \left(\frac{\partial G}{\partial \sigma}\right)_{\sigma=1}$, $c_4 = 1 - 2G(1) + \left(\frac{\partial G}{\partial \sigma}\right)_{\sigma=1}$, h is the boundary layer thickness (HBLT) and σ varies from 0 to 1. The boundary conditions of the shape function at $\sigma = 1$ are determined by the mixing below the boundary layer (see details in Large et al. (1994) and Appendix B in Van Roekel et al. (2018)).

From Equation 5, the response of nonlocal KPP flux to surface heat forcing can be broken down into a direct response through $Q_{\rm ns}$ and an indirect response through the shape function $G(\sigma)$. To diagnose the differences of direct and indirect response between HR and LR, we can rewrite the shape function and $Q_{\rm ns}$ in HR as $G_h = \Delta G + G_l$ and $Q_{\rm nsh} = \Delta Q_{\rm ns} + Q_{\rm nsl}$, where h and l represent HR and LR, respectively, and $\Delta(\cdot)$ denotes the difference between HR and LR. Therefore, the difference of nonlocal KPP flux between HR and LR can be expressed as

XU ET AL. 14 of 25

21699291, 2022, 12, Downloaded from https://agupubs.onlinelibrary.wiley.com/doi/10.1029/2022JC019065, Wiley Online Library on [11/01/2025]. See the Terms

conditions) on Wiley Online Library for rules of use; OA articles are governed by the applicable Creative Commons Licens

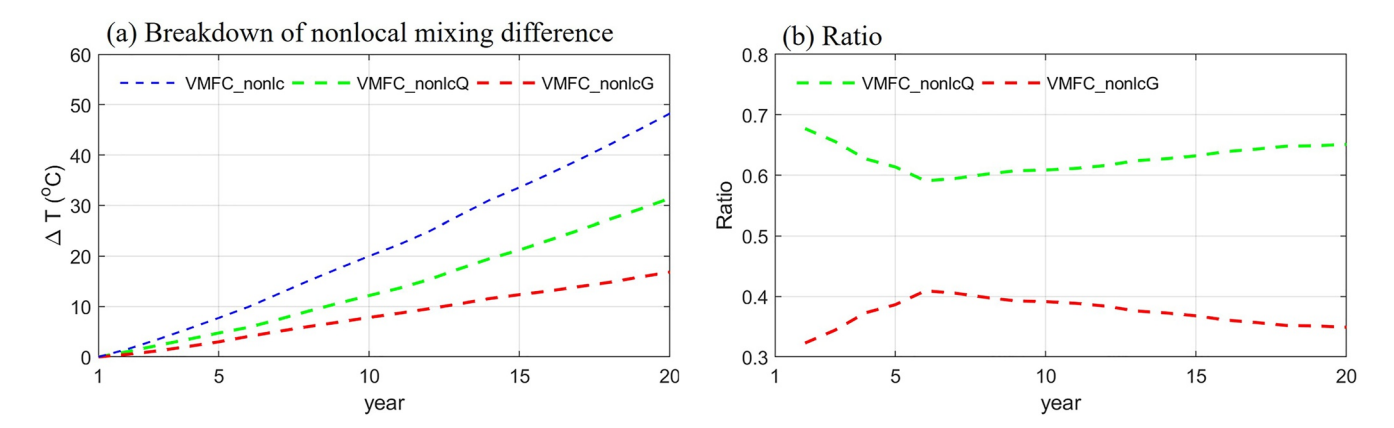


Figure 8. (a) Breakdown of VMFC_nonlc difference between SPIN-HR and SPIN-LR as shown in Figure 3d, blue dashed for VMFC_nonlc, green dashed for direct impact (VMFC_nonlcQ), red dashed for indirect impact (VMFC_nonlcG); (b) Ratio of VMFC_nonlcQ (green) and VMFC_nonlcG (red) over VMFC_nonlc difference between SPIN-HR and SPIN-LR. VMFC_nonlc is exactly the summation of VMFC_nonlcQ and VMFC_nonlcG.

$$(\kappa_z \gamma_x)_h - (\kappa_z \gamma_x)_l = C[(\Delta G + G_l)(\Delta Q_{\text{ns}} + Q_{\text{nsl}})] - CG_l Q_{\text{nsl}} = C[\Delta G Q_{\text{nsh}} + G_l \Delta Q_{\text{ns}}]. \tag{7}$$

On the right side of Equation 7, the first term represents the impact of changes of shape function in HR from LR, which includes the negligible cross term (indirect response, hereafter VMFC_nonlcG), and the second term represents the impact of differences of non-shortwave heat flux (direct response, hereafter VMFC_nonlcQ).

Figure 8a presents the breakdown of globally averaged VMFC_nonlc differences between SPIN-HR and SPIN-LR, clearly showing that the direct response (i.e., VMFC_nonlcQ) is larger than the indirect response (i.e., VMFC_nonlcG). The 20-year mean of VMFC_nonlcQ is 14.01°C, accounting for 63% of the total VMFC_nonlc difference. The ratio of VMFC_nonlcQ and VMFC_nonlcG over VMFC_nonlc are shown in Figure 8b with green and red dashed lines, respectively. The contribution of VMFC_nonlcQ to VMFC_nonlc is between 60% and 70%.

Figures 9a and 9b display spatial patterns of the ratios of VMFC_nonlcQ over VMFC_nonlc and VMFC_nonlcG over VMFC_nonlc, respectively, for SPIN-HR minus SPIN-LR difference. In the eddy-active regions, VMFC_nonlcQ can explain more than 90% of VMFC_nonlc differences. However, in the regions where the Gulf Stream separates from the U.S. coast, contributions of VMFC_nonlcQ and VMFC_nonlcG to VMFC_nonlc are similar (50%). In the tropics, VMFC_nonlcQ and VMFC_nonlcG both play an important role, accounting for 60% and 40% of VMFC_nonlc differences, respectively. These results reveal that impacts of shape function cannot be neglected when we study the nonlocal KPP flux differences between HR and LR, indicating that oceanic

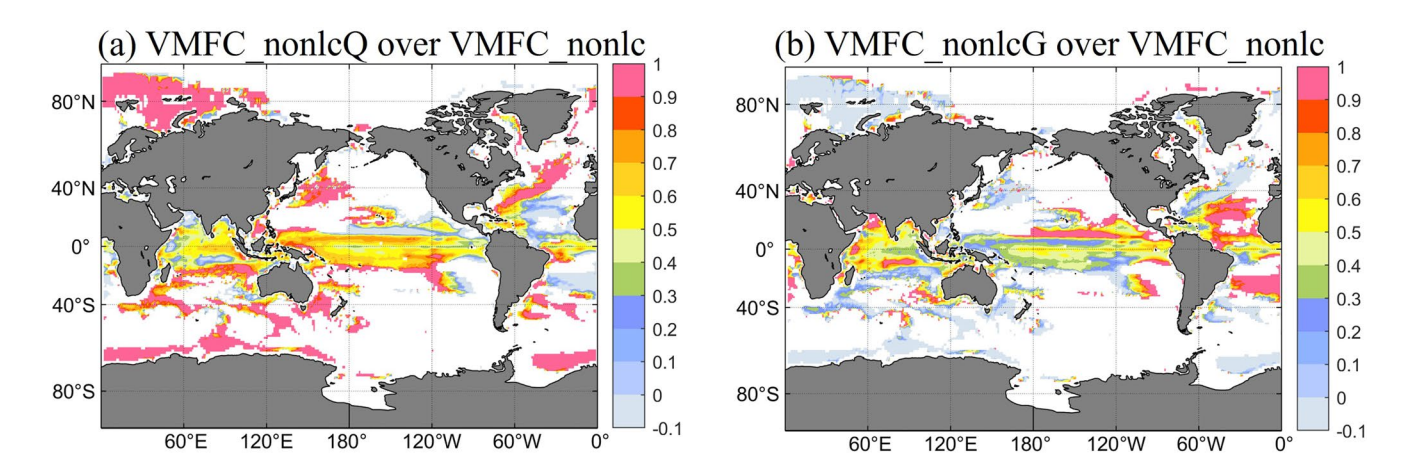


Figure 9. Ratio of 20-year averages for "SPIN-HR minus SPIN-LR" differences. (a) VMFC_nonlcQ over VMFC_nonlc, (b) VMFC_nonlcG over VMFC_nonlc. Only regions with positive difference of VMFC_nonlc between SPIN-HR and SPIN-LR (Figure 6d) are shown.

XU ET AL. 15 of 25

processes are also important in modulating nonlocal KPP fluxes. In the following, we will investigate how the shape function can differ between HR and LR.

As shown in Equation 6, the shape function is modulated by the boundary layer thickness, which is defined as the shallowest depth where the bulk Richardson number Ri_b (refer to Equation 21 in Large et al., 1994) reaches 0.3. By definition, Ri_b can be influenced by the surface buoyancy forcing including freshwater and heat fluxes, indicating a nonlinear relationship between nonlocal KPP flux and surface heat flux. The shape function at 10 m can be estimated as ratio of the nonlocal KPP flux over the non-shortwave heat flux using monthly model output. It is clearly shown that the shape function varies strongly with respect to non-shortwave heat flux in both the tropics and eddy-active regions (Figures 10a–10c), confirming that nonlocal KPP flux is not a nonlinear function of non-shortwave heat flux.

To mathematically quantify the nonlinearity, binned averages of the estimated shape function in the three regions are shown as dots with bin width of 5 W/m² in Figures 10d–10f, and solid lines are the corresponding quartic fits to the data. The fitting coefficients are labeled in the legends in each panel. Results indicate that shape function is highly nonlinear in the large Q_{ns} regime ($\geq 200 \text{ W/m}^2$) in both HR (red) and LR (blue). It is also shown that LR is less capable of simulating extremely strong Q_{ns} in the tropics ($\geq 750 \text{ W/m}^2$) and KE ($\geq 800 \text{ W/m}^2$). In these extreme Q_{ns} regimes, the shape function shows higher values in HR than LR, suggesting large contribution of shape function to nonlocal KPP flux difference between HR and LR. The possible oceanic processes that give rise to this nonlinearity will be discussed in the following section.

5.1.2. Role of Eddies in Nonlocal KPP Mixing

The fitting polynomial shown in Figure 10 is a mathematical approximation of the relationship between the shape function and non-shortwave heat flux, and so it likely differs from the shape function computed in CESM. Nevertheless, this simple analysis shows that the shape function is a nonlinear function of non-shortwave heat flux, indicating that it is difficult to precisely decompose nonlocal KPP flux differences into contributions from the shape function and the surface heat flux. However, as shown in Equation 6, the shape function is modulated by HBLT, which is determined by the bulk Richardson number, indicating that oceanic processes can modulate the nonlinear relationship of shape function and Q_{ns} through local heat distributions. Vertical heat transport (VHT) in the ocean acts to redistribute heat, which impacts the bulk Richardson number. As shown in Wolfe et al. (2008), mean-flow induced vertical heat transport (MVHT) is downward and eddy-induced vertical heat transport (EVHT) is upward in the global average, a result also seen in other studies (Brierley et al., 2010; Griffies et al., 2015; Hieronymus & Nycander, 2013; Jing et al., 2020; Su et al., 2018, 2020; von Storch et al., 2016). To shed light on the influence of VHT on nonlocal KPP flux, we conducted sensitivity experiments by changing the strength of the submesoscale parameterization in LR CESM. In this parameterization, a parameter that controls the strength of submesoscale parameterization is the horizontal length scale (HLS) of the fronts (Fox-Kemper et al., 2011). Experiments with smaller HLS have stronger submesoscale eddy fluxes in the extratropics. The default value is 5 km (EXP5km), and we conducted two sensitivity experiments with HLS reduced to 3 km for 50 years (EXP3km) and 800 m (EXP800m) for 20 years. Both of these runs started from the first day of CNTL-LR and other model settings were kept the same.

The 50-year averaged results in EXP5km and EXP3km are shown in Figure 11. As demonstrated in Figure 11a, MVHT averaged over the combined KE ($145^{\circ}-170^{\circ}E$, $34^{\circ}-39^{\circ}N$) and GSE ($65^{\circ}-50^{\circ}W$, $33^{\circ}-41^{\circ}N$) region is slightly changed from EXP5km to EXP3km, but EVHT shows a significant increase with a maximum of 12.69 W/m² at 60 m (about 29.7% of EVHT in EXP5km). Figure 11b shows nonlocal KPP flux, $Q_{\rm net}$, shortwave heat flux (SW), and HBLT in KE and GSE in EXP5km (blue) and EXP3km (cyan) on the left y-axis, as well as their difference (red) on the right y-axis. Nonlocal KPP flux is increased by 4% (4.16 W/m²), and HBLT is decreased by 7% (3.99 m) from EXP5km to EXP3km. Similar results for 20-year mean in EXP5km, EXP3km, and EXP800m are shown in Figure S10 in Supporting Information S1. Nonlocal KPP flux (HBLT) keeps increasing (decreasing) from EXP5km, EXP3km to EXP800, indicating that the response of nonlocal KPP flux and HBLT to EVHT are monotonic. In contrast, $Q_{\rm net}$ is strengthened by about 2% (Figure 11b) or 3% (Figure S10b in Supporting Information S1) from EXP5km to EXP3km, but it is weakened by 3.6% (Figure S10b in Supporting Information S1) from EXP3km to EXP800m. In addition, SW shows little changes across three experiments. Therefore, the atmospheric response to submesoscale parameterization is weaker.

XU ET AL. 16 of 25

21699291, 2022, 12, Downloaded from https://agupubs.onlinelibrary.wiley.com/doi/10.10292022LC019065, Wiley Online Library on [11/01/2025]. See the Terms and Conditions (https://onlinelibrary.wiley.com/terms-and-conditions) on Wiley Online Library for rules of use; OA articles are governed by the applicable Creative Commons Licensensand Conditions (https://onlinelibrary.wiley.com/terms-and-conditions) on Wiley Online Library for rules of use; OA articles are governed by the applicable Creative Commons Licensensand Conditions (https://onlinelibrary.wiley.com/terms-and-conditions) on Wiley Online Library for rules of use; OA articles are governed by the applicable Creative Commons Licensensand Conditions (https://onlinelibrary.wiley.com/terms-and-conditions) on Wiley Online Library for rules of use; OA articles are governed by the applicable Creative Commons Licensensand Conditions (https://onlinelibrary.wiley.com/terms-and-conditions) on Wiley Online Library for rules of use; OA articles are governed by the applicable Creative Commons Licensensand Conditions (https://onlinelibrary.wiley.com/terms-and-conditions) on Wiley Online Library for rules of use; OA articles are governed by the applicable Creative Commons Licensensand Conditions (https://onlinelibrary.wiley.com/terms-and-conditions) on Wiley Online Library for rules of use; OA articles are governed by the applicable Creative Commons Licensensand Conditions (https://onlinelibrary.wiley.com/terms-and-conditions) on Wiley Online Library for rules of use; OA articles are governed by the applicable Creative Commons Licensensand Conditions (https://onlinelibrary.wiley.com/terms-and-conditions) on Wiley Online Library for rules of use; OA articles are governed by the applicable Creative Commons Licensensand Conditions (https://onlinelibrary.wiley.com/terms-and-conditions) on Wiley Online Library for rules of use; OA articles are governed by the applicable Creative Commons Licensensand Conditions (https://onlinelibrary.wiley.com/terms-and-conditions) on Wiley Onli

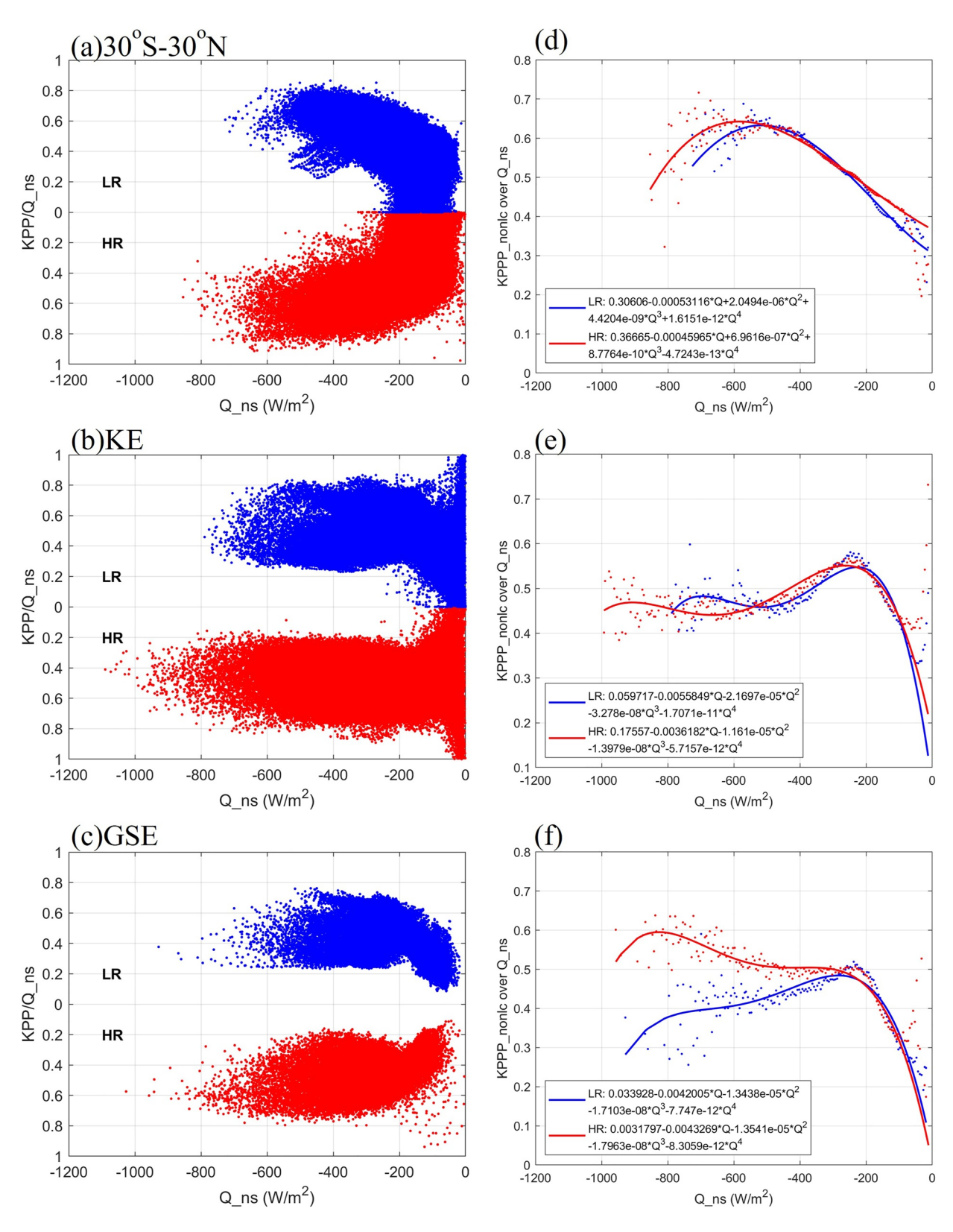


Figure 10. Shape function at 10 m as a function of Q_{ns} in (a) tropics, (b) Kuroshio extension (KE), and (c) Gulf Stream extension (GSE); heat flux-binned shape function in (d) tropics, (e) KE, and (f) GSE, each bin with width of 5 W/m². Dots for CESM results, solid lines for quartic fitting. Red for SPIN-HR and blue for SPIN-LR.

XU ET AL. 17 of 25

21699291, 2022, 12, Downloaded from https://agupubs.onlinelibrary.wiley.com/doi/10.1029/2022JC019065, Wiley Online Library on [11/01/2025]. See the Terms and Conditions (https://agupubs.onlinelibrary.wiley.com/doi/10.1029/2022JC019065, Wiley Online Library on [11/01/2025]. See the Terms and Conditions (https://agupubs.onlinelibrary.wiley.com/doi/10.1029/2022JC019065, Wiley Online Library on [11/01/2025]. See the Terms and Conditions (https://agupubs.onlinelibrary.wiley.com/doi/10.1029/2022JC019065, Wiley Online Library on [11/01/2025]. See the Terms and Conditions (https://agupubs.onlinelibrary.wiley.com/doi/10.1029/2022JC019065, Wiley Online Library on [11/01/2025]. See the Terms and Conditions (https://agupubs.onlinelibrary.wiley.com/doi/10.1029/2022JC019065, Wiley Online Library.wiley.com/doi/10.1029/2022JC019065, Wiley Online Library.wiley.com/doi/10.1029/2022JC019066, Wiley Online Library.wiley.com/doi/10.1029/2022JC019066, Wiley Online Library.wiley.wiley.com/doi/10.1029/2022JC019066, Wiley Online Library.wiley.com/doi/10.1029/2022JC019066, Wiley Online Library.wiley.wiley.wiley.com/doi/10.1029/2022JC019066, Wiley Online Library.wiley.wi

and-conditions) on Wiley Online Library for rules of use; OA articles are governed by the applicable Creative Commons Licenso

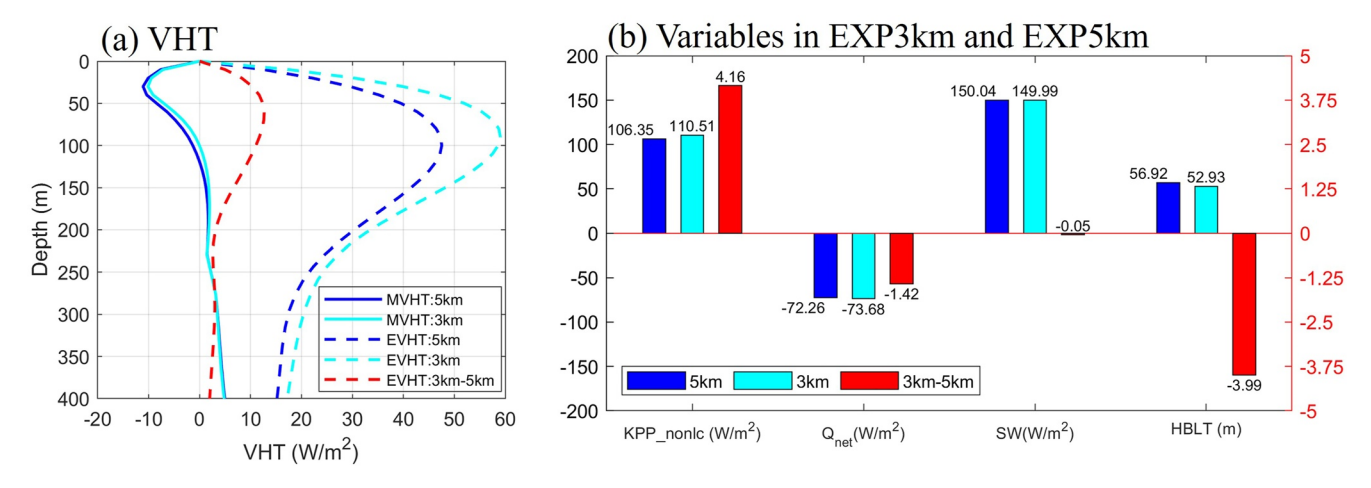


Figure 11. Fifty-year averaged (a) MVHT (solid) and EVHT (dashed) from EXP5km (blue), EXP3km (cyan), and EXP3km minus EXP5km (red); (b) nonlocal KPP flux, Q_{net} , SW at the surface, and HBLT from EXP5km (blue) and EXP3km (cyan) on the left y-axis, and EXP3km minus EXP5km (red) on the right y-axis. Results are combined over KE ($145^{\circ}-170^{\circ}\text{E}$, $34^{\circ}-39^{\circ}\text{N}$) and GSE ($65^{\circ}-50^{\circ}\text{W}$, $33^{\circ}-41^{\circ}\text{N}$). Units are shown in brackets following each variable.

The EVHT and nonlocal KPP flux changes can be connected as follows. From Figure 11a, it is clear that there is a stronger VHT-induced local warming above 60 m and stronger VHT-induced local cooling below 60 m from EXP5km to EXP3km because the difference of EVHT reaches maximum at 60 m, indicating a more thermally stratified upper ocean in EXP3km. Therefore, HBLT is shallower in EXP3km than EXP5km. This result also holds at 20 years for these simulations as well as between EXP3km and EXP800m shown in Figure S10a. As a consequence, the stronger warming between 10 and 60 m in EXP3km and EXP800m can provide more heat to the top 10 m for nonlocal KPP mixing.

Although HBLT is not saved in the output in CNTL-HR and CNTL-LR-HRIC, we can check the difference in temperature at 45 m (T45m) between CNTL-HR and CNTL-LR-HRIC as shown in Figure 12a. It is clear that the T45m is warmer in CNTL-HR than CNTL-LR-HRIC in most regions, especially in eddy-active regions (also true in SPIN-HR and SPIN-LR, Figure S11 in Supporting Information S1), indicating there is more heat for nonlocal KPP mixing to move into the upper 10 m in HR than LR. In line with the finding in Jing et al. (2020), we propose the mechanism of nonlocal KPP mixing modulating SST as follows. As shown in Figure 12b, the surface heat loss will lead to strong eddy vertical heat transport (w'T') based on the theory in Jing et al. (2020). Since w'T' peaks around 50 m (Jing et al., 2020) and decreases to zero at the sea surface, the heat convergence by w'T' is greatest between 10 and 50 m, which can be regarded as a heat reservoir for the upper 10 m. Based on Figures 4g and 12b, the cooling at the surface and the warming below 10 m are both stronger in HR than LR, which feeds a stronger

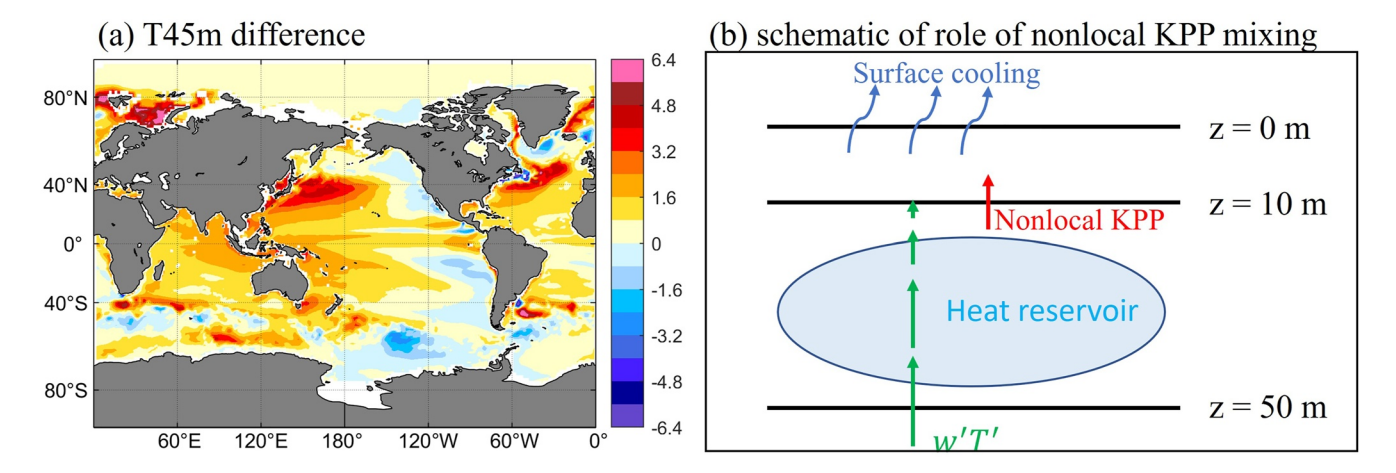


Figure 12. (a) T45m (°C) difference between CNTL-HR and CNTL-LR-HRIC; (b) schematic of role of nonlocal KPP mixing in modulating SST.

XU ET AL. 18 of 25

2169291, 2022, 12, Downloaded from https://agupubs.online.library.wiley.com/doi/10.1029/2022/C019065, Wiley Online Library on [11/01/2025]. See the Terms and Conditions (https://onlinelibrary.wiley.com/terms-and-conditions) on Wiley Online Library for rules of use; OA articles are governed by the applicable Creative Commons Licensens and Conditions (https://onlinelibrary.wiley.com/terms-and-conditions) on Wiley Online Library for rules of use; OA articles are governed by the applicable Creative Commons Licensens and Conditions (https://onlinelibrary.wiley.com/terms-and-conditions) on Wiley Online Library for rules of use; OA articles are governed by the applicable Creative Commons Licensens and Conditions (https://onlinelibrary.wiley.com/terms-and-conditions) on Wiley Online Library for rules of use; OA articles are governed by the applicable Creative Commons Licensens and Conditions (https://onlinelibrary.wiley.com/terms-and-conditions) on Wiley Online Library for rules of use; OA articles are governed by the applicable Creative Commons Licensens and Conditions (https://onlinelibrary.wiley.com/terms-and-conditions) on Wiley Online Library for rules of use; OA articles are governed by the applicable Creative Commons Licensens and Conditions (https://onlinelibrary.wiley.com/terms-and-conditions) on Wiley Online Library for rules of use; OA articles are governed by the applicable Creative Commons (https://onlinelibrary.wiley.com/terms-and-conditions) on Wiley Online Library for rules of use; OA articles are governed by the applicable Creative Commons (https://onlinelibrary.wiley.com/terms-and-conditions) on Wiley Online Library for rules of use; OA articles are governed by the applicable Creative Commons (https://onlinelibrary.wiley.com/terms-and-conditions) on Wiley Online Library for rules of use; OA articles are governed by the applicable Creative Commons (https://onlinelibrary.wiley.com/terms-and-conditions) on Wiley Online Library for rules of use; OA articles are governed by the applicable Creative Commons

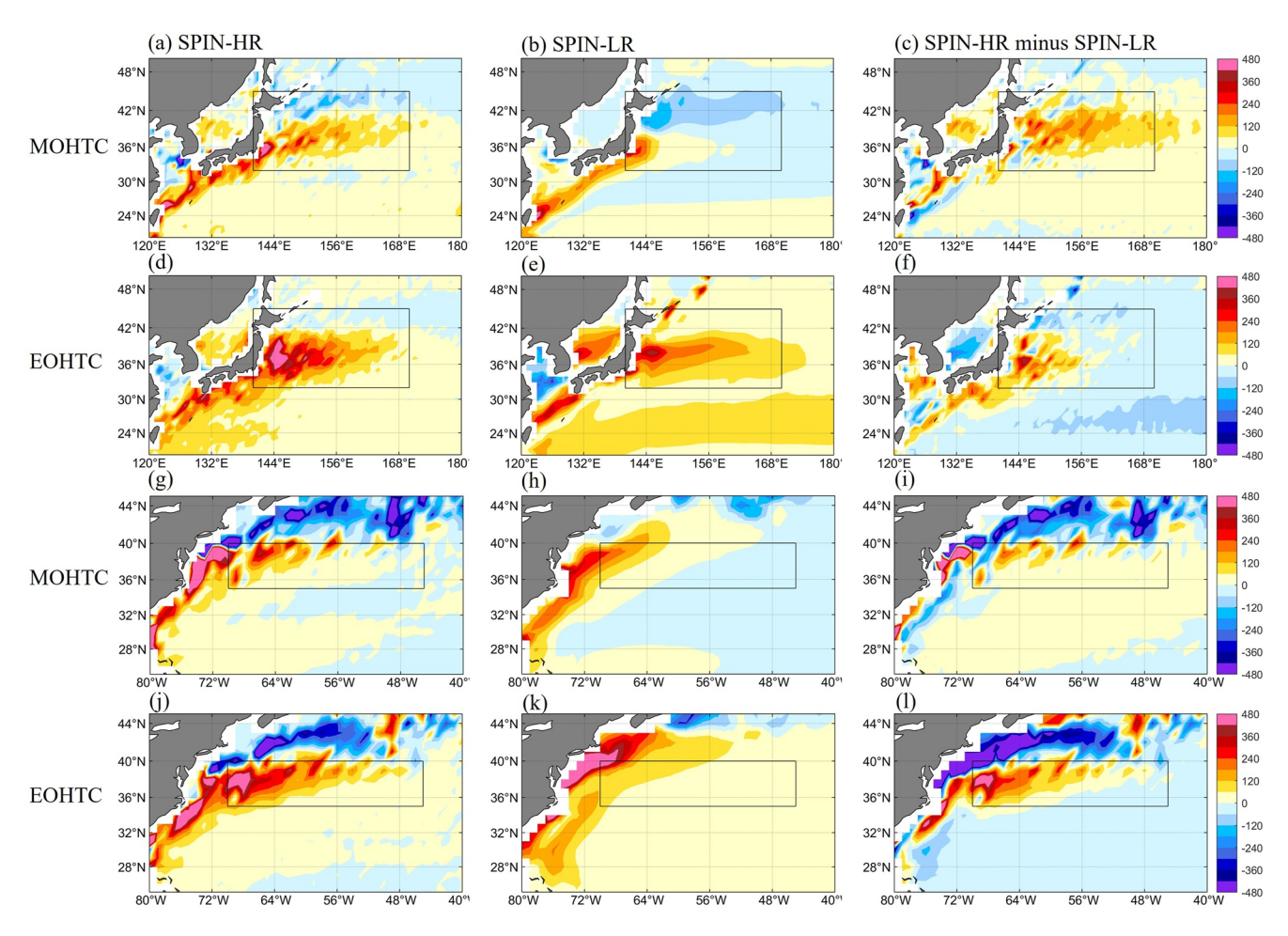


Figure 13. Mean-flow and eddy-induced components of Ocean Heat Transport Convergence in SPIN-HR (first column), SPIN-LR (second column), and their differences SPIN-HR minus SPIN-LR (third column). (a–f) for Kuroshio extension, (g–l) for Gulf Stream extension. Units for MOHTC and EOHTC: °C.

nonlocal KPP flux, bringing more heat to the upper 10 m. Although nonlocal KPP flux is parametrized in CESM, the determination of HBLT is essentially a reflection of this physical process.

5.2. Ocean Advection

OHTC, including horizontal and vertical components, is the second largest factor in generating warmer SST in HR in eddy-active regions (Figure 7a), corresponding to 62% of the contribution from VMFC_nonlc. OHTC is further decomposed into mean-flow-induced OHTC (MOHTC) and eddy-induced OHTC (EOHTC), where eddies are defined as the deviation from the monthly mean in HR and as parameterized eddies in LR. Since KE and GSE are the two largest eddy-active regions, analysis in this section will be mainly focused on KE and GSE.

Differences of MOHTC and EOHTC between SPIN-HR and SPIN-LR in KE and GSE are shown in Figure 13. As in Figure 4, the boxes delineate regions where OHTC in HR and LR show large differences. In KE, the warming induced by MOHTC extends more northward and eastward compared with LR (Figures 13a and 13b), leading to warmer MOHTC-related SST difference between HR and LR in the boxed region (Figure 13c). In contrast, EOHTC in HR and LR shares a similar spatial pattern in KE (Figures 13d and 13e), but produces a stronger warming in HR in the region where the Kuroshio current separates from Japan (Figure 13f). In the boxed region, MOHTC tends to generate 69.51°C warmer SST in SPIN-HR than SPIN-LR, which is more than 8 times larger than the contribution from EOHTC (8.42°C).

In GSE, MOHTC and EOHTC in LR both reflect a more severe overshoot of the Gulf Stream (Figures 13j and 13k) compared with HR (Figures 13g and 13h) (see also Small, Bacmeister, et al., 2014). The improved

XU ET AL. 19 of 25

21699291, 2022, 12, Downloaded from https://agupubs.onlinelibrary.wiley.com/doi/10.1029/2022JC019065, Wiley Online Library on [11/01/2025]. See the Terms and Conditions (http://doi.org/10.1029/2022JC019065, Wiley Online Library on [11/01/2025].

on Wiley Online Library for rules of use;

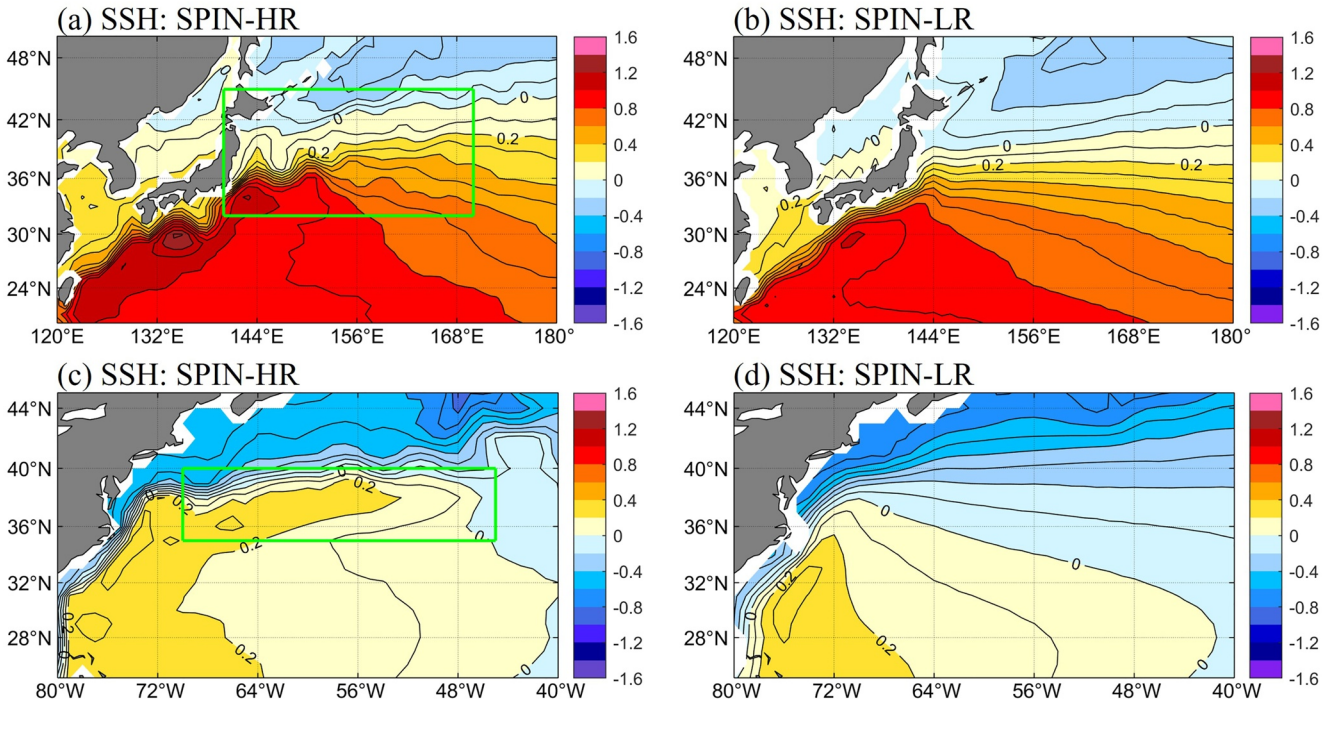


Figure 14. Sea surface height in (a) and (b) Kuroshio extension and in (c) and (d) Gulf Stream extension from SPIN-HR and SPIN-LR. Units: m.

Gulf Stream in HR explains the dipole pattern in the differences of MOHTC and EOHTC between HR and LR (Figures 13i and 13l). In contrast to KE, MOHTC in the GSE box only contributes to warmer SST by 32.75°C (Figure 13i), which is smaller than the contribution from EOHTC (58.27°C, Figure 13l).

To investigate in more detail the mean circulation in KE and GSE, SSH is shown in Figure 14. In KE, the boundary between the subpolar and subtropical gyres is along 42°N in SPIN-HR, which is to the north of that in SPIN-LR (zero lines in Figures 14a and 14b). In addition, the strength of currents offshore of Japan is greater in SPIN-HR than SPIN-LR, as is the strength of recirculation flow. These differences lead to more warm water advected into the boxed region in SPIN-HR than SPIN-LR. In GSE, the recirculation in SPIN-HR is stronger and extends further eastward than in SPIN-LR. The overshoot problem is improved in SPIN-HR, which is consistent with the advection patterns in Figures 13j and 13k. The improvement of the Gulf Stream in POP2 simulations has also been noted by Bryan et al. (2007) by increasing horizontal resolution to 0.1°. They showed that the separation of the GS is sensitive to dissipation parameter choices. As summarized in Chassignet and Marshall (2008), there are many other factors that can influence the GS separation, for instance, subpolar gyre strength, Deep western boundary current, and representation of topography.

6. Summary and Discussion

6.1. Summary

A recent study by Ma et al. (2021) showed that CMIP6 models share the same SST biases as previous CMIP5 models. Given that these two generations of climate models have similar horizontal resolution of \sim 1°, it raises the question of how SST biases are related to model resolution in these climate models. The present study attempts to address this question by analyzing the HighResMIP multi-model ensemble, which is a new model intercomparison project endorsed by CMIP6, aimed at assessing the impacts of climate model horizontal resolution on climate simulations. We particularly focus on examination of a set of HighResMIP simulations conducted by iHESP using CESM1.3, which includes a pair of 106-year high- and low-resolution control simulations (CNTL-HR and CNTL-LR-HRIC), and another pair of 20-year high- and low-resolution spin-up simulations (SPIN-HR and SPIN-LR). In each pair, the simulations have the same temperature and salinity initial conditions, so that initial state differences will not have an impact on ocean heat budget analysis. Seven other eddy-resolving

XU ET AL. 20 of 25



Journal of Geophysical Research: Oceans

10.1029/2022JC019065

and eddy-permitting models in the HighResMIP ensemble, including HadGEM3-GC3.1, AWI-CM-1-1, and ECMWF-IFS, are also analyzed and compared to CESM1.3. The results confirm that increasing model resolution can substantially reduce SST biases, including the warm bias in EBUS and cold bias in the western basins and tropics. The focus of this study is on the cold bias as it has not been thoroughly investigated by previous studies.

To investigate SST bias differences between HR and LR, both globally averaged and spatial surface ocean heat budget analyses are applied to the simulations. The globally averaged heat budget analysis reveals that the heat balance in the uppermost 10 m is mainly between atmospheric fluxes (i.e., AFC) and oceanic vertical mixing (i.e., VMFC) in both HR and LR, while vertical advection (i.e., VHTC) plays a secondary role. At the surface, non-shortwave heat flux cools the ocean. The solar radiation absorbed in the top 10 m cannot completely compensate the cooling induced by non-shortwave heat flux. Therefore, vertical mixing is important to close the budget by generating warming in the upper 10 m. Further decomposition indicates that it is the convective heat flux that accounts for the warming in the top 10 m through nonlocal vertical mixing from the subsurface to the uppermost layer. The differences of heat budget terms between HR and LR suggest that it is shortwave heat flux and nonlocal vertical mixing that account for the 1°C warmer global SST in HR.

Spatial surface ocean heat budget analysis demonstrates that stronger nonlocal KPP mixing (i.e., VMFC nonlo) and shortwave heat flux (i.e., AFC_SW) in HR are mainly located in the eddy-active regions and the tropics, but the dominant term differs between eddy-active regions and the tropics. In the eddy-active regions, VMFC_nonlc (160.1°C) contributes the most to warmer SST in HR, followed by OHTC (98.9°C) and AFC SW (23.6°C), and the importance of the latter is different from the globally averaged results. Further analysis shows that the stronger VMFC_nonlc in eddy-active regions in HR is mainly induced by the direct impact of non-shortwave heat flux instead of indirect impact via changes in the shape function. Regarding OHTC, it is found that the improvements in the strengths and positions of the western boundary currents favor warmer SST in HR, especially in KE and GSE. In the tropics, VMFC_nonlc and AFC_SW both contribute to warmer SST in HR by 45.5 and 53.7°C, respectively, consistent with the globally averaged results. The stronger AFC SW is likely induced by fewer clouds in HR, which may be related to model resolution impacts on cloud parameterizations. In contrast to eddy-active regions, both the direct and indirect impact of non-shortwave heat flux on nonlocal KPP flux contribute to the warmer SST in HR, accounting for 60% and 40%, respectively, of the nonlocal VMFC difference between HR and LR. It is also confirmed that the shape function responds to surface heat flux forcing in a nonlinear manner in both eddy-active regions and tropics, indicating that oceanic processes can strongly modulate the shape function. Based on three submesoscale parameterization sensitivity experiments, we proposed that the eddy induced vertical heat transport below 10 m can modulate nonlocal KPP mixing in the top 10 m.

6.2. Discussion

The comparison between HR and LR demonstrates that increasing horizontal resolutions can lead to SST bias reduction. One new result from this study is the important role of nonlocal KPP mixing in reducing the cold SST bias over much of the tropical and midlatitude oceans as model horizontal resolution increases. This is somewhat unexpected, as KPP is a vertical mixing parameterization. As such, it is expected that KPP is sensitive to vertical resolutions (Jia et al., 2021), but not necessarily horizontal resolution. With a finer vertical resolution, SST in the central equatorial Pacific is found to get warmer due to changes in vertical diffusivity (Jia et al., 2021). However, the vertical resolution is kept the same in HR and LR CESM, indicating that KPP also depends on horizontal resolutions. As model horizontal resolution increases, mesoscale features, including fronts and eddies, are explicitly represented in HR, which can have an impact on boundary layer thickness, and thus the non-local KPP. This then raises a question of whether KPP needs to be re-tuned when model horizontal resolution is changed while keeping vertical resolution intact. This issue needs to further be investigated by conducting model sensitivity experiments with HR configuration to better understand the role of KPP in simulating realistic SST. It is also worth noting that, based on a recent study by Van Roekel et al. (2018), the nonlocal KPP needs further improvements. Therefore, the role of the non-local KPP in SST simulations may be changed as its parameterization is improved.

Although HadGEM3-GC3.1, AWI-CM-1.1, and ECMWF-IFS show SST differences between high-resolution and low-resolution simulations that are consistent with CESM, only AWI-CM-1.1 employs the same vertical mixing parameterization as in CESM while the other two use a turbulent kinetic energy (TKE) parameterization. In the TKE scheme, turbulent tracer flux is nonzero only with nonzero vertical gradient of mean quantities, which

XU ET AL. 21 of 25

21699291, 2022, 12, Downloaded from https://agupubs.onlinelibrary.wiley.com/doi/10.1029/2022JC019065, Wiley Online Library on [11/01/2025]. See the Terms

on Wiley Online Library for rules of use; OA articles are governed by the applicable Creative Commons Licenso

is not determined by the surface buoyancy forcing at all (Pandey & Dwivedi, 2021). Therefore, more analysis should be conducted to confirm the impact of vertical mixing on the SST difference between high-resolution and low-resolution HadGEM3-GC3.1 and ECMWF-IFS. The dominant component of non-shortwave heat flux difference between LR and HR is the latent heat flux, especially in the midlatitudes. Wu et al. (2019) showed that the latent heat flux becomes stronger in the midlatitudes as they increase the atmosphere resolution from 130, 60, 25 km using the atmosphere component of Met Office's Unified Model. Minobe et al. (2008) pointed out that sharp SST gradients are vital to generate surface wind convergence which induces a stronger latent heat flux. Small, Tomas, and Bryan (2014) also confirmed that SST fronts can modulate turbulent heat fluxes through changes of the surface stability using CAM4. Although previous studies were based on atmosphere only experiments, they provide hints that differences of turbulent heat fluxes between LR and HR are highly associated with SST fronts in the midlatitudes, which needs more analyses in future work.

In the Southern Ocean, changes in SST from LR to HR (Figure 4) cannot be explained by nonlocal KPP mixing (Figure 6). There, a strong compensation between vertical mixing and non-shortwave heat flux is found with complex spatial structures in HR (Figure 4g and 4h). In CMIP5 models, the warm SST biases have been attributed to cloud errors over the Southern Ocean (Hyder et al., 2018). In LR, the shortwave cloud-SST feedback is positive almost everywhere in the Southern Ocean (Bacmeister et al., 2020), but in HR it is weaker and more complex (Figure S12 in Supporting Information S1). The positive feedback in HR is found in a region east of 180° in the Pacific sector with reduced strength compared to LR. HR also shows negative feedback between SST and clouds in the Indian and Atlantic sector, which is fundamentally different from LR. Therefore, increasing horizontal resolution in CESM does have significant impacts on the SST-cloud feedback in the Southern Ocean. Given that the positive shortwave cloud-SST feedback is reduced in HR, it is possible that the larger positive SST bias in HR may be caused by the reduced cooling effect of the shortwave cloud forcing on SST. However, a future in-depth investigation is needed to further understand the SST bias difference between HR and LR in the Southern Ocean.

As discussed in Chang et al. (2020), it is a more formidable challenge to tune model parameters in HR than in LR due to the combined factor of the exceedingly high computational cost and the need for many iterations of order 30–50-year simulations with small adjustments in model parameters. For this reason, the HR presented in this study has not been extensively tuned, particularly, the parameterizations related to atmospheric deep convection and cloud processes that directly impact the shortwave radiation, and thus SST bias. It is entirely possible that some of the SST biases, such as those in the Southern Ocean, can be reduced by re-tuning model's cumulus and cloud parameterizations.

Though the Gulf Stream path is improved from LR to HR CESM, it is still not realistic in HR. A recent inter-model comparation study by Chassignet et al. (2020) shows this problem is not unique to POP2. Chassignet and Xu (2017) argue that the horizontal resolution of 0.1° may not be sufficient to fully resolve the Rossby radius of deformation at two grid points (Hallberg, 2013), thereby baroclinic instability. A horizontal resolution of 0.02° is required to fully resolve dynamical processes associated with submesoscale eddies, leading to a more realistic simulation of the Gulf Stream (Chassignet & Xu, 2017). For global Earth system models, such a high horizontal resolution at 0.02° will carry prohibitively high computational cost. Therefore, it will be necessary to further optimize sub-grid parameterizations, including vertical mixing and submesoscale eddy parameterizations, in mesoscale-eddy-resolving models.

Data Availability Statement

CNTL-HR is available at http://esgf-data.dkrz.de/search/cmip6-dkrz/?mip_era=CMIP6&activity_id=High-ResMIP&institution_id=NCAR&source_id=CESM1-CAM5-SE-HR&experiment_id=control-1950. CNTL-LR-HRIC, SPIN-HR and SPIN-LR are available from the authors on request. Analyses are conducted using NCL and Matlab.

References

Ashfaq, M., Skinner, C. B., & Diffenbaugh, N. S. (2011). Influence of SST biases on future climate change projections. *Climate Dynamics*, 36(7–8), 1303–1319. https://doi.org/10.1007/s00382-010-0875-2

Bacmeister, J. T., Hannay, C., Medeiros, B., Gettelman, A., Neale, R., Fredriksen, H. B., et al. (2020). CO₂ increase experiments using the CESM: Relationship to climate sensitivity and comparison of CESM1 to CESM2. *Journal of Advances in Modeling Earth Systems*, 12(11), e2020MS002120. https://doi.org/10.1029/2020MS002120

Acknowledgments

This research uses simulations performed by the International Laboratory for High Resolution Earth System Prediction (iHESP)-a collaboration among the Qingdao National Laboratory for Marine Science and Technology (ONLM), Texas A&M University (TAMU), and the U.S. National Center for Atmospheric Research (NCAR). This research is partially supported by NSF Grant 2137684. NCAR is a major facility sponsored by the US NSF under Cooperative Agreement 1852977. G. Xu and Q. Zhang acknowledges the support from the China Scholarship Council. Authors thank Texas A&M University Supercomputing Facility. Special thanks go to Frederic Castruccio and Nan Rosenbloom for assistant in running the CESM simulations.

XU ET AL. 22 of 25

- Brierley, C. M., Collins, M., & Thorpe, A. J. (2010). The impact of perturbations to ocean-model parameters on climate and climate change in a coupled model. Climate Dynamics, 34(2), 325–343. https://doi.org/10.1007/s00382-008-0486-3
- Bryan, F. O., Hecht, M. W., & Smith, R. D. (2007). Resolution convergence and sensitivity studies with North Atlantic circulation models. Part I: The western boundary current system. *Ocean Modelling*, 16(3–4), 141–159. https://doi.org/10.1016/j.ocemod.2006.08.005
- Burls, N. J., Muir, L., Vincent, E. M., & Fedorov, A. (2017). Extra-tropical origin of equatorial Pacific cold bias in climate models with links to cloud albedo. Climate Dynamics, 49(5), 2093–2113. https://doi.org/10.1007/s00382-016-3435-6
- Camargo, S. J. (2013). Global and regional aspects of tropical cyclone activity in the CMIP5 models. *Journal of Climate*, 26(24), 9880–9902. https://doi.org/10.1175/JCLI-D-12-00549.1
- Chang, P., Zhang, S., Danabasoglu, G., Yeager, S. G., Fu, H., Wang, H., et al. (2020). An unprecedented set of high-resolution Earth system simulations for understanding multiscale interactions in climate variability and change. *Journal of Advances in Modeling Earth Systems*, 12(12), e2020MS002298. https://doi.org/10.1029/2020MS002298
- Chassignet, E. P., & Marshall, D. P. (2008). Gulf Stream separation in numerical ocean models. Geophysical Monograph Series, 177, 39–61. https://doi.org/10.1029/177GM05
- Chassignet, E. P., & Xu, X. (2017). Impact of horizontal resolution (1/12 to 1/50) on Gulf Stream separation, penetration, and variability. *Journal of Physical Oceanography*, 47(8), 1999–2021. https://doi.org/10.1175/JPO-D-17-0031.1
- Chassignet, E. P., Yeager, S. G., Fox-Kemper, B., Bozec, A., Castruccio, F., Danabasoglu, G., et al. (2020). Impact of horizontal resolution on global ocean–sea ice model simulations based on the experimental protocols of the Ocean Model Intercomparison Project Phase 2 (OMIP-2). Geoscientific Model Development, 13(9), 4595–4637. https://doi.org/10.5194/gmd-13-4595-2020
- Cherchi, A., Fogli, P. G., Lovato, T., Peano, D., Iovino, D., Gualdi, S., et al. (2019). Global mean climate and main patterns of variability in the CMCC-CM2 coupled model. *Journal of Advances in Modeling Earth Systems*, 11(1), 185–209. https://doi.org/10.1029/2018MS001369
- Danabasoglu, G., Bates, S. C., Briegleb, B. P., Jayne, S. R., Jochum, M., Large, W. G., et al. (2012). The CCSM4 ocean component. *Journal of Climate*, 25(5), 1361–1389. https://doi.org/10.1175/JCLI-D-11-00091.1
- Danabasoglu, G., Large, W. G., & Briegleb, B. P. (2010). Climate impacts of parameterized Nordic Sea overflows. *Journal of Geophysical Research*, 115(C11), C11005. https://doi.org/10.1029/2010JC006243
- Di Lorenzo, E., & Mantua, N. (2016). Multi-year persistence of the 2014/15 North Pacific marine heatwave. *Nature Climate Change*, 6(11), 1042–1047. https://doi.org/10.1038/nclimate3082
- Dutheil, C., Lengaigne, M., Bador, M., Vialard, J., Lefèvre, J., Jourdain, N. C., et al. (2020). Impact of projected sea surface temperature biases on tropical cyclones projections in the South Pacific. Scientific Reports, 10(1), 1–12. https://doi.org/10.1038/s41598-020-61570-6
- Fox-Kemper, B., Danabasoglu, G., Ferrari, R., Griffies, S. M., Hallberg, R. W., Holland, M. M., et al. (2011). Parameterization of mixed layer eddies. III: Implementation and impact in global ocean climate simulations. *Ocean Modelling*, 39(1–2), 61–78. https://doi.org/10.1016/j.ocemod.2010.09.002
- Fox-Kemper, B., Ferrari, R., & Hallberg, R. (2008). Parameterization of mixed layer eddies. Part I: Theory and diagnosis. *Journal of Physical Oceanography*, 38(6), 1145–1165. https://doi.org/10.1175/2007JPO3792.1
- Garfinkel, C. I., White, I., Gerber, E. P., & Jucker, M. (2020). The impact of SST biases in the tropical east Pacific and Agulhas current region on atmospheric stationary waves in the Southern Hemisphere. *Journal of Climate*, 33(21), 9351–9374. https://doi.org/10.1175/JCLI-D-20-0195.1
- Gent, P. R., & Mcwilliams, J. C. (1990). Isopycnal mixing in ocean circulation models. *Journal of Physical Oceanography*, 20(1), 150–155. https://doi.org/10.1175/1520-0485(1990)020<0150:IMIOCM>2.0.CO:2
- Gent, P. R., Yeager, S. G., Neale, R. B., Levis, S., & Bailey, D. A. (2010). Improvements in a half degree atmosphere/land version of the CCSM. Climate Dynamics. 34(6), 819–833. https://doi.org/10.1007/s00382-009-0614-8
- Good, S. A., Martin, M. J., & Rayner, N. A. (2013). EN4: Quality controlled ocean temperature and salinity profiles and monthly objective analyses with uncertainty estimates. *Journal of Geophysical Research: Oceans*, 118(12), 6704–6716. https://doi.org/10.1002/2013JC009067
- Griffies, S. M., Winton, M., Anderson, W. G., Benson, R., Delworth, T. L., Dufour, C. O., et al. (2015). Impacts on ocean heat from transient mesoscale eddies in a hierarchy of climate models. *Journal of Climate*, 28(3), 952–977. https://doi.org/10.1175/JCLI-D-14-00353.1
- Gutjahr, O., Putrasahan, D., Lohmann, K., Jungclaus, J. H., Storch, J. S. V., Brüggemann, N., et al. (2019). Max Planck Institute Earth System Model (MPI-ESM1.2) for the High-Resolution Model Intercomparison Project (HighResMIP). Geoscientific Model Development, 12(7), 3241–3281. https://doi.org/10.5194/gmd-12-3241-2019
- Haarsma, R., Acosta, M., Bakhshi, R., Bretonnière, P. A., Caron, L. P., Castrillo, M., et al. (2020). HighResMIP versions of EC-Earth: EC-Earth3P and EC-Earth3P-HR-description, model computational performance and basic validation. Geoscientific Model Development, 13(8), 3507–3527. https://doi.org/10.5194/gmd-2019-350
- Haarsma, R. J., Roberts, M. J., Vidale, P. L., Senior, C. A., Bellucci, A., Bao, Q., et al. (2016). High resolution model intercomparison project (HighResMIP v1. 0) for CMIP6. Geoscientific Model Development. 9(11), 4185–4208. https://doi.org/10.5194/gmd-9-4185-2016
- Hallberg, R. (2013). Using a resolution function to regulate parameterizations of oceanic mesoscale eddy effects. *Ocean Modelling*, 72, 92–103. https://doi.org/10.1016/j.ocemod.2013.08.007
- He, J., & Soden, B. J. (2016). The impact of SST biases on projections of anthropogenic climate change: A greater role for atmosphere-only models? Geophysical Research Letters, 43(14), 7745–7750. https://doi.org/10.1002/2016GL069803
- Hieronymus, M., & Nycander, J. (2013). The budgets of heat and salinity in NEMO. Ocean Modelling, 67, 28–38. https://doi.org/10.1016/j.ocemod.2013.03.006
- Hsu, W. C., Patricola, C. M., & Chang, P. (2019). The impact of climate model sea surface temperature biases on tropical cyclone simulations. Climate Dynamics, 53(1), 173–192. https://doi.org/10.1007/s00382-018-4577-5
- Hunke, E. C., & Lipscomb, W. H. (2008). CICE: The Los Alamos sea ice model user's manual, version 4. Los Alamos National Laboratory Technical Report (pp. 1–76). LA-CC-06-012.
- Hyder, P., Edwards, J. M., Allan, R. P., Hewitt, H. T., Bracegirdle, T. J., Gregory, J. M., et al. (2018). Critical Southern Ocean climate model biases traced to atmospheric model cloud errors. *Nature Communications*, 9(1), 1–17. https://doi.org/10.1038/s41467-018-05634-2
- Jia, Y., Richards, K. J., & Annamalai, H. (2021). The impact of vertical resolution in reducing biases in sea surface temperature in a tropical Pacific Ocean model. Ocean Modelling, 157, 101722. https://doi.org/10.1016/j.ocemod.2020.101722
- Jing, Z., Wang, S., Wu, L., Chang, P., Zhang, Q., Sun, B., et al. (2020). Maintenance of mid-latitude oceanic fronts by mesoscale eddies. *Science Advances*, 6(31), eaba7880, https://doi.org/10.1126/sciady.aba7880
- Johnson, N. C., Krishnamurthy, L., Wittenberg, A. T., Xiang, B., Vecchi, G. A., Kapnick, S. B., & Pascale, S. (2020). The impact of sea surface temperature biases on North American precipitation in a high-resolution climate model. *Journal of Climate*, 33(6), 2427–2447. https://doi. org/10.1175/JCLI-D-19-0417.1
- Kirtman, B. P., Bitz, C., Bryan, F., Collins, W., Dennis, J., Hearn, N., et al. (2012). Impact of ocean model resolution on CCSM climate simulations. Climate Dynamics, 39(6), 1303–1328. https://doi.org/10.1007/s00382-012-1500-3

XU ET AL. 23 of 25

- Kurian, J., Li, P., Chang, P., Patricola, C. M., & Small, J. (2021). Impact of the Benguela coastal low-level jet on the southeast tropical Atlantic SST bias in a regional ocean model. *Climate Dynamics*, 56(9–10), 1–28. https://doi.org/10.1007/s00382-020-05616-5
- Large, W. G., & Danabasoglu, G. (2006). Attribution and impacts of upper-ocean biases in CCSM3. Journal of Climate, 19(11), 2325–2346. https://doi.org/10.1175/JCL13740.1
- Large, W. G., McWilliams, J. C., & Doney, S. C. (1994). Oceanic vertical mixing: A review and a model with a nonlocal boundary layer parameterization. Reviews of Geophysics, 32(4), 363–403. https://doi.org/10.1029/94RG01872
- Lawrence, D. M., Oleson, K. W., Flanner, M. G., Thornton, P. E., Swenson, S. C., Lawrence, P. J., et al. (2011). Parameterization improvements and functional and structural advances in version 4 of the Community Land Model. *Journal of Advances in Modeling Earth Systems*, 3(1). https://doi.org/10.1029/2011MS00045
- Lee, R. W., Woollings, T. J., Hoskins, B. J., Williams, K. D., O'Reilly, C. H., & Masato, G. (2018). Impact of Gulf Stream SST biases on the global atmospheric circulation. Climate Dynamics, 51(9), 3369–3387. https://doi.org/10.1007/s00382-018-4083-9
- Li, G., & Xie, S. P. (2012). Origins of tropical-wide SST biases in CMIP multi-model ensembles. Geophysical Research Letters, 39(22). https://doi.org/10.1029/2012GL053777
- Liu, X., Ma, X., Chang, P., Jia, Y., Fu, D., Xu, G., et al. (2021). Ocean fronts and eddies force atmospheric rivers and heavy precipitation in western North America. Nature Communications, 12(1), 1–10. https://doi.org/10.1038/s41467-021-21504-w
- Ma, H. Y., Siongco, A. C., Klein, S. A., Xie, S., Karspeck, A. R., Raeder, K., et al. (2021). On the correspondence between seasonal forecast biases and long-term climate biases in sea surface temperature. *Journal of Climate*, 34(1), 427–446. https://doi.org/10.1175/JCLI-D-20-0338.1
- Ma, J., Xu, S., & Wang, B. (2019). Warm bias of sea surface temperature in eastern boundary current regions—A study of effects of horizontal resolution in CESM. Ocean Dynamics, 69(8), 939–954. https://doi.org/10.1007/s10236-019-01280-4
- Marzocchi, A., Hirschi, J. J. M., Holliday, N. P., Cunningham, S. A., Blaker, A. T., & Coward, A. C. (2015). The North Atlantic subpolar circulation in an eddy-resolving global ocean model. *Journal of Marine Systems*, 142, 126–143. https://doi.org/10.1016/j.jmarsys.2014.10.007
- McCabe, G. J., Palecki, M. A., & Betancourt, J. L. (2004). Pacific and Atlantic Ocean influences on multidecadal drought frequency in the United States. *Proceedings of the National Academy of Sciences*, 101(12), 4136–4141. https://doi.org/10.1073/pnas.0306738101
- McGregor, S., Stuecker, M. F., Kajtar, J. B., England, M. H., & Collins, M. (2018). Model tropical Atlantic biases underpin diminished Pacific decadal variability. *Nature Climate Change*, 8(6), 493–498, https://doi.org/10.1038/s41558-018-0163-4
- McPhaden, M. J., Zebiak, S. E., & Glantz, M. H. (2006). ENSO as an integrating concept in Earth science. Science, 314(5806), 1740–1745. https://doi.org/10.1126/science.1132588
- Meehl, G. A., Yang, D., Arblaster, J. M., Bates, S. C., Rosenbloom, N., Neale, R., et al. (2019). Effects of model resolution, physics, and coupling on Southern Hemisphere storm tracks in CESM1. 3. Geophysical Research Letters, 46(21), 12408–12416. https://doi.org/10.1029/2019GL084057
- Minobe, S., Kuwano-Yoshida, A., Komori, N., Xie, S. P., & Small, R. J. (2008). Influence of the Gulf Stream on the troposphere. *Nature*, 452(7184), 206–209. https://doi.org/10.1038/nature06690
- Moum, J. N., Perlin, A., Nash, J. D., & McPhaden, M. J. (2013). Seasonal sea surface cooling in the equatorial Pacific cold tongue controlled by ocean mixing. *Nature*, 500(7460), 64–67. https://doi.org/10.1038/nature12363
- Neale, R. B., Chen, C. C., Gettelman, A., Lauritzen, P. H., Park, S., Williamson, D. L., & Taylor, M. A. (2010). Description of the NCAR community atmosphere model (CAM 5.0). NCAR Technical Note NCAR/TN-486+ STR, 1(1), 1–12.
- Pandey, L. K., & Dwivedi, S. (2021). Comparing the performance of turbulent kinetic energy and k-profile parameterization vertical parameterization schemes over the tropical Indian Ocean. *Marine Geodesy*, 44(1), 42–69. https://doi.org/10.1080/01490419.2020.1835758
- Rackow, T., Sein, D. V., Semmler, T., Danilov, S., Koldunov, N. V., Sidorenko, D., et al. (2019). Sensitivity of deep ocean biases to horizontal resolution in prototype CMIP6 simulations with AWI-CM1. 0. Geoscientific Model Development, 12(7), 2635–2656. https://doi.org/10.5194/ gmd-12-2635-2019
- Rayner, N. A. A., Parker, D. E., Horton, E. B., Folland, C. K., Alexander, L. V., Rowell, D. P., & Kaplan, A. (2003). Global analyses of sea surface temperature, sea ice, and night marine air temperature since the late nineteenth century. *Journal of Geophysical Research*, 108(D14), 4407. https://doi.org/10.1029/2002JD002670
- Reynolds, R. W., & Smith, T. M. (1994). Improved global sea surface temperature analyses using optimum interpolation. *Journal of Climate*, 7(6), 929–948. https://doi.org/10.1175/1520-0442(1994)007<0929:IGSSTA>2.0.CO;2
- Roberts, C. D., Senan, R., Molteni, F., Boussetta, S., Mayer, M., & Keeley, S. P. (2018). Climate model configurations of the ECMWF integrated forecasting system (ECMWF-IFS cycle 43r1) for HighResMIP. *Geoscientific Model Development*, 11(9), 3681–3712. https://doi.org/10.5194/gmd-11-3681-2018
- Roberts, M. J., Baker, A., Blockley, E. W., Calvert, D., Coward, A., Hewitt, H. T., et al. (2019). Description of the resolution hierarchy of the global coupled HadGEM3-GC3.1 model as used in CMIP6 HighResMIP experiments. *Geoscientific Model Development*, 12(12), 4999–5028. https://doi.org/10.5194/gmd-12-4999-2019
- Roemmich, D., Johnson, G. C., Riser, S., Davis, R., Gilson, J., Owens, W. B., et al. (2009). The Argo Program: Observing the global ocean with profiling floats. *Oceanography*, 22(2), 34–43. https://doi.org/10.5670/oceanog.2009.36
- Semmler, T., Danilov, S., Rackow, T., Sidorenko, D., Hegewald, J., Sein, D., et al. (2017). AWI AWI-CM 1.1 HR model output prepared for CMIP6 HighResMIP. Earth System Grid Federation. Retrieved from http://cera-www.dkrz.de/WDCC/meta/CMIP6/CMIP6.HighResMIP. AWI.AWI-CM-1-1-HR
- Small, R. J., Bacmeister, J., Bailey, D., Baker, A., Bishop, S., Bryan, F., et al. (2014). A new synoptic scale resolving global climate simulation using the Community Earth System Model. *Journal of Advances in Modeling Earth Systems*, 6(4), 1065–1094. https://doi.org/10.1002/2014MS000363
- Small, R. J., Curchitser, E., Hedstrom, K., Kauffman, B., & Large, W. G. (2015). The Benguela upwelling system: Quantifying the sensitivity to resolution and coastal wind representation in a global climate model. *Journal of Climate*, 28(23), 9409–9432. https://doi.org/10.1175/ JCLI-D-15-0192.1
- Small, R. J., Tomas, R. A., & Bryan, F. O. (2014). Storm track response to ocean fronts in a global high-resolution climate model. Climate Dynamics, 43(3–4), 805–828. https://doi.org/10.1007/s00382-013-1980-9
- Smith, R., Jones, P., Briegleb, B., Bryan, F., Danabasoglu, G., Dennis, J., et al. (2010). The parallel ocean program (POP) reference manual ocean component of the community climate system model (CCSM) and community Earth system model (CESM). LAUR-01853, 141, 1–140.
- Smith, S. R., Alory, G., Andersson, A., Asher, W., Baker, A., Berry, D. I., et al. (2019). Ship-based contributions to global ocean, weather, and climate observing systems. Frontiers in Marine Science, 6, 434. https://doi.org/10.3389/fmars.2019.00434
- Song, X., & Zhang, G. J. (2009). Convection parameterization, tropical Pacific double ITCZ, and upper-ocean biases in the NCAR CCSM3. Part I: Climatology and atmospheric feedback. *Journal of Climate*, 22(16), 4299–4315. https://doi.org/10.1175/2009JCLI2642.1

XU ET AL. 24 of 25



Journal of Geophysical Research: Oceans

- 10.1029/2022JC019065
- Su, Z., Torres, H., Klein, P., Thompson, A. F., Siegelman, L., Wang, J., et al. (2020). High-frequency submesoscale motions enhance the upward vertical heat transport in the global ocean. *Journal of Geophysical Research: Oceans*, 125(9), e2020JC016544. https://doi.org/10.1029/2020JC016544
- Su, Z., Wang, J., Klein, P., Thompson, A. F., & Menemenlis, D. (2018). Ocean submesoscales as a key component of the global heat budget. Nature Communications, 9(1), 1–8. https://doi.org/10.1038/s41467-018-02983-w
- Vannière, B., Guilyardi, E., Toniazzo, T., Madec, G., & Woolnough, S. (2014). A systematic approach to identify the sources of tropical SST errors in coupled models using the adjustment of initialised experiments. *Climate Dynamics*, 43(7), 2261–2282. https://doi.org/10.1007/s00382-014-2051-6
- Van Roekel, L., Adcroft, A. J., Danabasoglu, G., Griffies, S. M., Kauffman, B., Large, W., et al. (2018). The KPP boundary layer scheme for the ocean: Revisiting its formulation and benchmarking one-dimensional simulations relative to LES. *Journal of Advances in Modeling Earth Systems*, 10(11), 2647–2685. https://doi.org/10.1029/2018MS001336
- Voldoire, A., Saint-Martin, D., Sénési, S., Decharme, B., Alias, A., Chevallier, M., et al. (2019). Evaluation of CMIP6 deck experiments with CNRM-CM6-1. *Journal of Advances in Modeling Earth Systems*, 11(7), 2177–2213. https://doi.org/10.1029/2019MS001683
- von Storch, J. S., Haak, H., Hertwig, E., & Fast, I. (2016). Vertical heat and salt fluxes due to resolved and parameterized meso-scale eddies. Ocean Modelling, 108, 1–19. https://doi.org/10.1016/j.ocemod.2016.10.001
- Wang, C., Zhang, L., Lee, S. K., Wu, L., & Mechoso, C. R. (2014). A global perspective on CMIP5 climate model biases. *Nature Climate Change*, 4(3), 201–205. https://doi.org/10.1038/nclimate2118
- Woelfle, M. D., Yu, S., Bretherton, C. S., & Pritchard, M. S. (2018). Sensitivity of coupled tropical Pacific model biases to convective parameterization in CESM1. Journal of Advances in Modeling Earth Systems, 10(1), 126–144. https://doi.org/10.1002/2017MS001176
- Wolfe, C. L., Cessi, P., McClean, J. L., & Maltrud, M. E. (2008). Vertical heat transport in eddying ocean models. *Geophysical Research Letters*, 35(23), L23605, https://doi.org/10.1029/2008GL036138
- Woodruff, S. D., Diaz, H. F., Worley, S. J., Reynolds, R. W., & Lubker, S. J. (2005). Early ship observational data and ICOADS. *Climatic Change*, 73(1), 169–194. https://doi.org/10.1007/s10584-005-3456-3
- Wu, P., Roberts, M., Martin, G., Chen, X., Zhou, T., & Vidale, P. L. (2019). The impact of horizontal atmospheric resolution in modelling air–sea heat fluxes. *Quarterly Journal of the Royal Meteorological Society*, 145(724), 3271–3283. https://doi.org/10.1002/qj.3618
- Xu, Z., Chang, P., Richter, I., & Tang, G. (2014). Diagnosing southeast tropical Atlantic SST and ocean circulation biases in the CMIP5 ensemble. Climate Dynamics, 43(11), 3123–3145. https://doi.org/10.1007/s00382-014-2247-9
- Ying, J., Huang, P., Lian, T., & Tan, H. (2019). Understanding the effect of an excessive cold tongue bias on projecting the tropical Pacific SST warming pattern in CMIP5 models. Climate Dynamics, 52(3), 1805–1818. https://doi.org/10.1007/s00382-018-4219-y
- Zhang, L., & Zhao, C. (2015). Processes and mechanisms for the model SST biases in the north Atlantic and north Pacific: A link with the a tlantic
- meridional overturning circulation. *Journal of Advances in Modeling Earth Systems*, 7(2), 739–758. https://doi.org/10.1002/2014MS000415 Zhang, R., Delworth, T. L., Rosati, A., Anderson, W. G., Dixon, K. W., Lee, H. C., & Zeng, F. (2011). Sensitivity of the North Atlantic Ocean circulation to an abrupt change in the Nordic Sea overflow in a high resolution global coupled climate model. *Journal of Geophysical Research*, 116(C12), C12024. https://doi.org/10.1029/2011JC007240
- Zhu, Y., Zhang, R. H., & Sun, J. (2020). North Pacific upper-ocean cold temperature biases in CMIP6 simulations and the role of regional vertical mixing. *Journal of Climate*, 33(17), 7523–7538. https://doi.org/10.1175/JCLI-D-19-0654.1

XU ET AL. 25 of 25